NON-OSCILLATORY CENTRAL SCHEMES FOR ONE- AND TWO-DIMENSIONAL MHD EQUATIONS. II: HIGH-ORDER SEMI-DISCRETE SCHEMES*

JORGE BALBÁS† AND EITAN TADMOR‡

Abstract. We present a new family of high-resolution, non-oscillatory semi-discrete central schemes for the approximate solution of the ideal Magnetohydrodynamics (MHD) equations. This is the second part of our work, where we are passing from the fully-discrete staggered schemes in [2] to the semi-discrete formulation advocated in [14]. This semi-discrete formulation retains the simplicity of fully-discrete central schemes while enhancing efficiency and adding versatility. The semi-discrete algorithm offers a wider range of options to implement its two key steps: non-oscillatory reconstruction of point values followed by the evolution of the corresponding point valued fluxes. We present the solution of several prototype MHD problems. Solutions of one-dimensional Brio-Wu shock-tube problems and the two-dimensional Kelvin-Helmholtz instability, Orszag-Tang vortex system, and the disruption of a high density cloud by a strong shock are carried out using third- and fourth-order central schemes based on the CWENO reconstructions. These results complement those presented in [2] and confirm the remarkable versatility and simplicity of central schemes as black-box, Jacobian-free MHD solvers. Furthermore, our numerical experiments demonstrate that this family of semi-discrete central schemes preserves the $\nabla \cdot \mathbf{B} = 0$-constraint within machine round-off error; happily, no constrained-transport enforcement is needed.

1. Introduction. In this paper we present third- and fourth-order accurate, non-oscillatory semi-discrete central schemes for the approximate solution of the equations of ideal Magnetohydrodynamics,

$$(1.1) \qquad \rho_t = -\nabla \cdot (\rho \mathbf{v}),$$

$$(1.2) \qquad (\rho \mathbf{v})_t = -\nabla \cdot [\rho \mathbf{v} \mathbf{v}^\top + (p + \frac{1}{2}B^2)I_{3\times 3} - \mathbf{B}\mathbf{B}^\top],$$

$$(1.3) \qquad \mathbf{B}_t = \nabla \times (\mathbf{v} \times \mathbf{B}),$$

$$(1.4) \qquad e_t = -\nabla \cdot \left[\left(\frac{\gamma}{\gamma - 1}p + \frac{1}{2}\rho v^2 \right) \mathbf{v} - (\mathbf{v} \times \mathbf{B}) \times \mathbf{B} \right].$$

Here, ρ and e are scalar quantities representing respectively, the mass density and the total internal energy, $\mathbf{v} = (v_x, v_y, v_z)^\top$ is the velocity field with *Euclidean* norm $v^2 := \|\mathbf{v}\|^2$, and $\mathbf{B} = (B_x, B_y, B_z)^\top$ and $B^2 := \|\mathbf{B}\|^2$ represent the magnetic field and its norm. The pressure, p, is coupled to the internal energy, $e = \frac{1}{2}\rho v^2 + \frac{1}{2}B^2 + p/(\gamma - 1)$, where γ is the (fixed) ratio of specific heats. The system is augmented by the solenoidal constraint,

$$(1.5) \qquad \nabla \cdot \mathbf{B} = 0;$$

that is, if the condition $\nabla \cdot \mathbf{B} = 0$ is satisfied initially at $t = 0$, then by (1.3) it remains invariant in time.

Our work [2] demonstrated the capability of central schemes to accurately and efficiently detect and resolve the steep gradients that characterize the solutions of (1.1)-(1.4); it suggested further development of higher order, black-box type central schemes for these equations. In this paper, we present a family of third- and fourth-order accurate, non-oscillatory semi-discrete central schemes which remain stable without any further

explicit enforcement of the constraint (1.5). This semi-discrete formulation, [14], retains the main advantages of central schemes over the upwind ones, namely, simplicity and efficiency resulting from the minimal amount of characteristic information required when evolving the solution over staggered grids, allowing for Jacobian-free formulations and avoiding dimensional splitting in multidimensional models. Moreover, semi-discrete schemes allow more flexibility in the calculation of the time step, Δt, than their fully-discrete counterparts: on the one hand, they are implemented over non-staggered grids, thus the CFL stability condition allows for the use of larger time steps, and on the other hand, for r^{th}-order methods, the numerical dissipation of the semi-discrete formulation is of order $\mathcal{O}((\Delta x)^{2r-1})$ *vs.* that of the corresponding fully-discrete version of order $\mathcal{O}((\Delta x)^{2r}/\Delta t)$; which allows the use of smaller time steps with considerably less smearing of discontinuities. Finally, the semi-discrete formulation also enjoys a remarkable adaptability to a wide range of non-oscillatory reconstruction techniques and evolution routines developed independently of the methods.

In addition to the five MHD prototype problems discussed in [2]: two one-dimensional Brio and Wu shock tube models originally proposed in [3], two different configurations — periodic and convective models — of the 2D transverse Kelvin-Helmholtz instability problem, and the 2D MHD vortex system of Orszag and Tang, we implement these new schemes to simulate the disruption of a high density cloud by a strong shock. The evolution of the Orszag–Tang vortex system involves the interaction between several shock waves traveling at various speed regimes, and the interaction between the high-density cloud and the strong shock describes a highly superfast flow, making both of these very suitable problems to test the robustness of numerical algorithms.

The paper is structured as follows:

In §2, we extend the derivation of the second- and third-order, central semi-discrete schemes presented in [14, 13, 12] to schemes of arbitrary order r. Starting with the staggered discretization that led to the fully-discrete central schemes, [20, 19, 10, 17], we evolve separately the smooth and non-smooth parts of the solution and project the resulting cell averages back onto the original grid. We then pass to the $\Delta t \downarrow 0$-limit, yielding the rth-order semi-discrete formulation of central schemes. This rather general formulation of central schemes entertains a broad range of options to implement the two main steps of the algorithm: non-oscillatory *reconstruction* of point values from cell averages, followed by the *evolution* of the corresponding point valued fluxes. In §3 we discuss the non-oscillatory reconstruction techniques and evolution routines that we implement to approximate the semi-discrete formulation of equations (1.1)–(1.4). For the reconstruction of point values, we propose an extension of the third-order Central WENO (CWENO) reconstruction of Kurganov and Levy, [12], and the *genuinely* two-dimensional fourth-order CWENO reconstruction of Levy et. al., [18], developed originally in the context of fully-discrete central schemes. For the evolution step, we use third- and fourth-order strong stability preserving (SSP) Runge-Kutta schemes, [23, 25, 5]. In §4 and §5 we describe the prototype MHD problems mentioned above and present the numerical solutions obtained with our new family of high resolution semi-discrete central schemes. In §4 we report on the one-dimensional shock tube problems of Brio and Wu [3] and discuss the improved resolution and better control of spurious oscillations provided by the new schemes. The two-dimensional test problems and the corresponding numerical results are presented and discussed in §5. These results confirm the efficiency of central schemes to accurately compute the solution of MHD equations. The combination of simplicity and high resolution allows us to obtain solutions comparable to those obtained with high order upwind schemes, e.g., [3, 4, 11, 22, 21], without having to refine the computational mesh as in [2]. We therefore retain the simplicity of central schemes — they eliminate the need for a detailed knowledge of the eigen-structure of the Jacobian matrices and avoid dimensional splitting and the costly use of (approximate) Riemann solvers that serve as building blocks for upwind schemes; at the same time, this simplicity is achieved without an increase in the computational work that was enforced by the finer meshes required with the lower order methods and/or any explicit enforcement of the solenoidal constraint $\nabla \cdot \mathbf{B} = 0$.

2. Semi-discrete Central Schemes. In [2] we demonstrated the robustness of black-box type central schemes to calculate the approximate solutions of equations (1.1)–(1.4) and discussed the advantages of these methods over those based on upwind differencing. We also pointed out, however, that the efficiency resulting

from a minimal amount of characteristic information required by central schemes, may be compromised by the low-order accuracy of the schemes, since the latter often require finer meshes to resolve steep gradients. In order to circumvent this limitation and gain full advantage of the simplicity, ease of implementation and efficiency of central schemes, we seek higher order methods. Although it is possible to carry out a higher order extension of the fully-discrete central schemes discussed in [2], see e.g., [16, 18], we find the semi-discrete formulation of Kurganov and Tadmor, [14], more advantageous: its implementation over non-staggered grids allows the use of larger time steps, it enjoys a reduced numerical dissipation (of order $\mathcal{O}((\Delta x)^{2r-1})$) in comparison to that of fully-discrete schemes ($\sim \mathcal{O}((\Delta x)^{2r}/\Delta t)$), and it is derived independently of any reconstruction or evolution algorithm. Indeed, many of the existing high-order, non-oscillatory reconstruction algorithms and evolution routines can be easily incorporated into the semi-discrete central formulation, making the simplicity and ease of implementation of central schemes an attractive alternative.

2.1. One-dimensional Schemes. The solutions of non-linear hyperbolic systems of conservation laws,

$$(2.1) \qquad u_t + f(u)_x = 0,$$

and in particular those of equations (1.1)–(1.4), are characterized by the onset and propagation of discontinuities. The higher order extensions of the first-order Lax-Friedrichs central scheme, [15], that have been developed over the past two decades, see e.g., [20, 19, 10, 14], provide a rather general approach for solving this type of problems with only a minimal amount of information on the eigen structure of the Jacobian matrix of $f(u)$ (indeed, Jacobian-free formulations of central schemes completely avoid the computation of $\frac{\partial f}{\partial u}$). These schemes are based on the evolution of the cell averages (we use the usual $\fint_I$ to denote the average, $1/|I| \cdot \int_I$),

$$\bar{u}_\alpha^n := \fint_{I_\alpha} u(\xi, t^n) d\xi, \qquad I_\alpha := [x_\alpha - \frac{\Delta x}{2}, x_\alpha + \frac{\Delta x}{2}]$$

while alternating over *staggered* grids, $\{I_j\} \times t^n$ and $\{I_{j+\frac{1}{2}}\} \times t^{n+1}$. Dividing (2.1) by Δx and integrating over the control volume $I_{j+\frac{1}{2}} \times [t^n, t^{n+1}]$ yields an exact discrete statement of the conservation law in terms of these cell averages,

$$(2.2) \qquad \bar{u}_{j+\frac{1}{2}}^{n+1} = \bar{u}_{j+\frac{1}{2}}^n - \frac{1}{\Delta x}\Big[\int_{t^n}^{t^{n+1}} f(u(x_{j+1}, \tau))d\tau - \int_{t^n}^{t^{n+1}} f(u(x_j, \tau))d\tau \Big].$$

The evaluation of the expressions on the right of (2.2) proceeds in two steps. First, the cell averages $\{\bar{u}_{j+\frac{1}{2}}^n\}$ are recovered by integrating a piecewise non-oscillatory polynomial reconstruction of the point-values of $u(x, t^n)$ from their cell averages $\{\bar{u}_j^n\}$ that we denote by

$$(2.3) \qquad u(x, t^n) = R(x; \bar{u}^n) := \sum_j p_j^n(x) \cdot \mathbf{1}_{I_j}.$$

This reconstruction procedure is at the heart of high-resolution, non-oscillatory central schemes, and requires the coefficients of the polynomials $\{p_j^n(x)\}$ to be determined so that $R(x; \bar{u}^n)$ satisfies the following three essential properties.

- $\mathcal{P}_1$ — Conservation of cell averages: $\bar{p}_j^n(x) = \bar{u}_j^n$.
- $\mathcal{P}_2$ — Accuracy: $R(x; \bar{u}^n) = u(x, t^n) + \mathcal{O}((\Delta x)^r)$ for r^{th}-order accurate scheme, wherever $u(\cdot, t^n)$ is sufficiently smooth.
- $\mathcal{P}_3$ — Non-oscillatory behavior of $\sum_j p_j(x) \cdot \mathbf{1}_{I_j}$ which is characterized in different ways for different reconstructions. Examples include TVD reconstructions initiated by van Leer and Harten, [27, 7], Number of Extrema Diminishing (NED) and shape preserving properties of Liu-Tadmor third order scheme, [19], and the higher order non-oscillatory extensions offered by the Essentially non-oscillatory (ENO) reconstructions of Harten et. al., e.g., [6], or their Weighted versions (WENO) e.g., [24, 9], and their implementation within the central differencing framework e.g., [12, 16, 18].
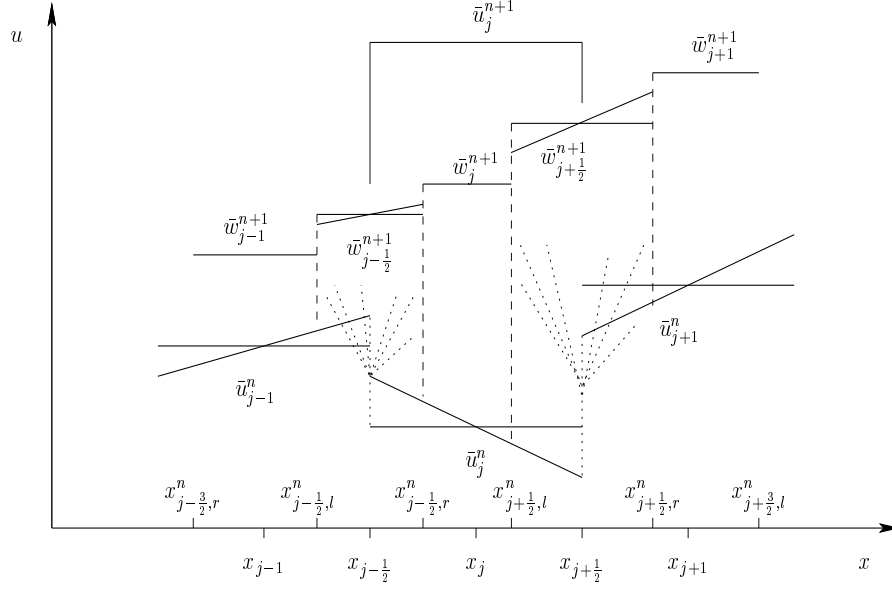
3

Fig. 2.1: Modified central differencing of Kurganov and Tadmor.

Equipped with the reconstructed point values $u(\cdot, t^n)$, the second step evaluates the two time integrals of $f(u(\cdot, \tau))$. Since the solution of (2.2) remains smooth along the lines $\{x = x_j\} \times [t^n, t^{n+1}]$, a simple quadrature rule suffices to approximate those integrals. This requires the intermediate values, $\{\bar{u}_j^{n+\beta}\}$, which are predicted either by a Taylor expansion or alternatively, by Runge-Kutta solvers of the ODE $u_\tau = \hat{f}_x|_{x=x_j}$, $u(x_j, 0) = u_j^n$, $\tau > t^n$, where $\hat{f}_x$ stands for the numerical derivative of $f(u)$. This type of evolution over staggered grids based on cells with uniform width Δx does not admit a semi-discrete limit as $\Delta t \downarrow 0$. Instead, a modified approach proposed by Kurganov and Tadmor in [14] and based on variable size cells (depicted in figure 2.1) yields the desired semi-discrete limit. Here, we extend the derivation of second- and third-order semi-discrete schemes of [14, 12, 13], to schemes of arbitrary order of accuracy r, [1]. The first step passing from a fully-discrete to a semi-discrete formulation, consists of reducing the size of the staggered cells covering the Riemann fans. Instead of cells with uniform width Δx, we use cells with variable width of order $\mathcal{O}(\Delta t)$, by incorporating the maximal local speed of propagation,

$$(2.4) \qquad a_{j+\frac{1}{2}}^n = \max_{u \in \mathcal{C}(u_{j+\frac{1}{2}}^-, u_{j+\frac{1}{2}}^+)} \rho\left(\frac{\partial f}{\partial u}(u)\right);$$

here $u_{j+\frac{1}{2}}^-$ and $u_{j+\frac{1}{2}}^+$ stand, respectively, for the reconstructed values of u to the left and right of the interfacing breakpoints, $u_{j+\frac{1}{2}}^\pm := R(x_{j+\frac{1}{2}}\pm, \bar{u}^n)$, and $\mathcal{C}$ is the phase curve connecting these two states through the Riemann fan. For practical purposes, we choose

$$a_{j+\frac{1}{2}}^n := \max\left\{\rho\left(\frac{\partial f}{\partial u}(u_{j+\frac{1}{2}}^-)\right), \rho\left(\frac{\partial f}{\partial u}(u_{j+\frac{1}{2}}^+)\right)\right\},$$

which is exact for genuinely non-linear and linearly degenerate fields.

4

This information allows us to repartition the original grid so as to distinguish between sub-cells of width $2a^n_{j+\frac{1}{2}}\Delta t^n$, where the solution is dictated by the non-smooth Riemann fan,

$$\widetilde{I}_{j+\frac{1}{2}} = [x^n_{j+\frac{1}{2},l},\ x^n_{j+\frac{1}{2},r}] := [x_{j+\frac{1}{2}} - a^n_{j+\frac{1}{2}}\Delta t^n,\ x_{j+\frac{1}{2}} + a^n_{j+\frac{1}{2}}\Delta t^n],$$

and the other cells of width $\Delta x_j := \Delta x - \Delta t^n(a^n_{j-\frac{1}{2}} + a^n_{j+\frac{1}{2}})$, which are beyond the influence of the Riemann fans so that the solution remains smooth,

$$\widetilde{I}_j = [x^n_{j-\frac{1}{2},r},\ x^n_{j+\frac{1}{2},l}] := [x_{j-\frac{1}{2}} + a^n_{j-\frac{1}{2}}\Delta t^n,\ x_{j+\frac{1}{2}} - a^n_{j+\frac{1}{2}}\Delta t^n].$$

In non-smooth regions, the cell averages, $\{\bar{w}^{n+1}_{j+\frac{1}{2}}\}$ are computed via staggered evolution over the (narrower, $\mathcal{O}(\Delta t)$) cells covering the Riemann fans,

$$\bar{w}^{n+1}_{j+\frac{1}{2}} := \int_{x^n_{j+\frac{1}{2},l}}^{x^n_{j+\frac{1}{2},r}} u(x, t^{n+1})dx =$$

(2.5)
$$= \int_{x^n_{j+\frac{1}{2},l}}^{x^n_{j+\frac{1}{2},r}} R\ (x; \bar{u}^n)dx - \frac{1}{2a^n_{j+\frac{1}{2}}}\int_{t^n}^{t^{n+1}} \left[f(u(x^n_{j+\frac{1}{2},r}, \tau)) - f(u(x^n_{j+\frac{1}{2},l}, \tau))\right]d\tau,$$

and in the smooth regions, direct integration of (2.1) yields the cell averages $\{\bar{w}^n_j\}$

$$\bar{w}^{n+1}_j := \int_{x^n_{j-\frac{1}{2},r}}^{x^n_{j+\frac{1}{2},l}} u(x, t^{n+1})dx =$$

(2.6)
$$= \int_{x^n_{j-\frac{1}{2},r}}^{x^n_{j+\frac{1}{2},l}} R\ (x; \bar{u}^n)dx - \frac{1}{\Delta x_j}\int_{t^n}^{t^{n+1}} \left[f(u(x^n_{j+\frac{1}{2},l}, \tau)) - f(u(x^n_{j-\frac{1}{2},r}, \tau))\right]d\tau.$$

The *non-staggered* cell averages, $\{\bar{u}^{n+1}_j\}$, are then recovered via a new non-oscillatory piecewise polynomial reconstruction of the point values of $u(x, t^{n+1})$ from the new cell averages (2.5) and (2.6),

(2.7)
$$R\ (x; \bar{w}^{n+1}) = \sum_j q^{n+1}_j(x) \cdot \mathbf{1}_{\widetilde{I}_j} + q^{n+1}_{j+\frac{1}{2}}(x) \cdot \mathbf{1}_{\widetilde{I}_{j+\frac{1}{2}}}.$$

Projection onto the original grid, $\{I_j\}$, (2.7) yields

$$\bar{u}^{n+1}_j := \int_{x_{j-\frac{1}{2}}}^{x_{j+\frac{1}{2}}} R\ (x; \bar{w}^{n+1})dx =$$

(2.8)
$$= \frac{1}{\Delta x}\left[\int_{x_{j-\frac{1}{2}}}^{x_{j-\frac{1}{2},r}} q^{n+1}_{j-\frac{1}{2}}(x)\ dx + \int_{x_{j-\frac{1}{2},r}}^{x_{j+\frac{1}{2},l}} q^{n+1}_j(x)\ dx + \int_{x_{j+\frac{1}{2},l}}^{x_{j+\frac{1}{2}}} q^{n+1}_{j+\frac{1}{2}}(x)\ dx\right].$$

The explicit calculation of the polynomials $q^{n+1}_j(x)$ and $q^{n+1}_{j+1/2}(x)$ will, in fact, prove to be irrelevant for the semi-discrete formulation that we seek. As we shall see below, only the *cell averages* of these q's matter, and in the $\Delta t \downarrow 0$-limit, these averages are further reduced to the original point values reconstructed at the interfaces, $p(x_{j\pm\frac{1}{2}}, t^n)$. We turn to the details. Without loss of generality, we assume that the q^{n+1}'s are polynomials of degree $r - 1$ (required to preserve the underlying r^{th}-order accuracy) and satisfy properties $\mathcal{P}_1 - \mathcal{P}_3$ for the cell averages (2.5) and (2.6) in the corresponding cells $\widetilde{I}_j$ and $\widetilde{I}_{j+\frac{1}{2}}$. We express these polynomials as

5

$q_{j\pm\frac{1}{2}}^{n+1}(x) = \sum_{k=0}^{r-1} A_{j\pm\frac{1}{2}}^{(k)}(x-x_{j\pm\frac{1}{2}})^k/k!$; their coefficients can be uniquely determined by imposing the conservation constraints[1],

$$(2.9) \qquad \fint_{\widetilde{I}_{j+p}} q_{j+s}^{n+1}(x)dx = \bar{w}_{j+p}^n, \qquad p = 0, \pm\frac{1}{2}, \pm 1, \ldots, \pm\frac{r-1}{2}, \qquad s = -\frac{1}{2}, 0, \frac{1}{2}.$$

Equipped with this notation, the first and last integrals on the right of (2.8) read

$$(2.10) \qquad \int_{x_{j-\frac{1}{2}}}^{x_{j-\frac{1}{2}},r} q_{j-\frac{1}{2}}^{n+1}(x)\, dx = \sum_{k=0}^{r-1} \left[\frac{A_{j-\frac{1}{2}}^{(k)}}{(k+1)!}(x - x_{j-\frac{1}{2}})^{k+1} \right]_{x_{j-\frac{1}{2}}}^{x_{j-\frac{1}{2}}+a_{j-\frac{1}{2}}^n \Delta t} = \sum_{k=0}^{r-1} \frac{(\Delta t)^{k+1}}{(k+1)!}(a_{j-\frac{1}{2}}^n)^{k+1} A_{j-\frac{1}{2}}^{(k)},$$

and

$$(2.11) \qquad \int_{x_{j+\frac{1}{2}},l}^{x_{j+\frac{1}{2}}} q_{j+\frac{1}{2}}^{n+1}(x)\, dx = \sum_{k=0}^{r-1} \left[\frac{A_{j+\frac{1}{2}}^{(k)}}{(k+1)!}(x - x_{j+\frac{1}{2}})^{k+1} \right]_{x_{j+\frac{1}{2}}-a_{j+\frac{1}{2}}^n \Delta t}^{x_{j+\frac{1}{2}}} = \sum_{k=0}^{r-1} (-1)^k \frac{(\Delta t)^{k+1}}{(k+1)!}(a_{j+\frac{1}{2}}^n)^{k+1} A_{j+\frac{1}{2}}^{(k)}.$$

For the second integral in (2.8), we observe that by property $\mathcal{P}_1$ the polynomial $q_j^{n+1}(x)$ must satisfy

$$(2.12) \qquad \int_{x_{j-\frac{1}{2}},r}^{x_{j+\frac{1}{2}},l} q_j^{n+1}(x)\, dx = \Delta x_j \bar{w}_j^{n+1} = \left[\Delta x - \Delta t(a_{j-\frac{1}{2}}^n + a_{j+\frac{1}{2}}^n) \right] \bar{w}_j^{n+1}.$$

Substituting (2.10)–(2.12) into (2.8), we arrive at a fully-discrete, non-staggered approximation (of arbitrary order of accuracy r) of the cell averages in (2.2),

$$(2.13)$$
$$\bar{u}_j^{n+1} = \sum_{k=0}^{r-1} \frac{\lambda(\Delta t)^k}{(k+1)!} \left[(a_{j-\frac{1}{2}}^n)^{k+1} A_{j-\frac{1}{2}}^{(k)} + (-1)^k (a_{j+\frac{1}{2}}^n)^{k+1} A_{j+\frac{1}{2}}^{(k)} \right] + \left[1 - \lambda(a_{j-\frac{1}{2}}^n + a_{j+\frac{1}{2}}^n) \right] \bar{w}_j^{n+1}, \quad \lambda := \frac{\Delta t}{\Delta x}.$$

Given the appropriate reconstructions $R(x; \bar{u}^n)$, $R(x; \bar{w}^n)$, and quadrature rules to evaluate the flux integrals in (2.5) and (2.6), then (2.13) constitutes a family of fully-discrete non-oscillatory central schemes, e.g., [8, 14]. This type of schemes admit a considerably simpler and more versatile semi-discrete limit, $d\bar{u}_j/dt := \lim_{\Delta t \to 0}(\bar{u}_j(t^n + \Delta t) - \bar{u}_j(t^n))/\Delta t$.

To this end, we rewrite (2.13) as

$$(2.14)$$
$$\frac{d\bar{u}_j}{dt} = \lim_{\Delta t \to 0} \left\{ \frac{1}{\Delta x}(a_{j-\frac{1}{2}}^n A_{j-\frac{1}{2}}^{(0)} + a_{j+\frac{1}{2}}^n A_{j+\frac{1}{2}}^{(0)}) + \frac{1}{\Delta t}(\bar{w}_j^{n+1} - \bar{u}_j^n) - \frac{1}{\Delta x}(a_{j-\frac{1}{2}}^n + a_{j+\frac{1}{2}}^n)\bar{w}_j^{n+1} \right.$$
$$\left. + \sum_{k=1}^{r-1} \frac{\lambda(\Delta t)^{k-1}}{(k+1)!} \left[(a_{j-\frac{1}{2}}^n)^{k+1} A_{j-\frac{1}{2}}^{(k)} + (-1)^k (a_{j+\frac{1}{2}}^n)^{k+1} A_{j+\frac{1}{2}}^{(k)} \right] \right\} =$$
$$= \lim_{\Delta t \to 0} \left\{ \frac{1}{\Delta x}(a_{j-\frac{1}{2}}^n A_{j-\frac{1}{2}}^{(0)} + a_{j+\frac{1}{2}}^n A_{j+\frac{1}{2}}^{(0)}) + \frac{1}{\Delta t}(\bar{w}_j^{n+1} - \bar{u}_j^n) - \frac{1}{\Delta x}(a_{j-\frac{1}{2}}^n + a_{j+\frac{1}{2}}^n)\bar{w}_j^{n+1} \right\}.$$

Since the width of the local Riemann fans approaches zero in the $\Delta t \downarrow 0$-limit, i.e., $x_{j+\frac{1}{2},l}^n, x_{j+\frac{1}{2},r}^n \to x_{j+\frac{1}{2}}$, we obtain by conservation of cell averages property $\mathcal{P}_1$, $A_{j\pm\frac{1}{2}}^{(0)} = \bar{w}_{j\pm\frac{1}{2}}^{n+1}$ so that (2.14) yields,

$$(2.15) \qquad \frac{d\bar{u}_j}{dt} = \lim_{\Delta t \to 0} \left\{ \frac{1}{\Delta x}(a_{j-\frac{1}{2}}^n \bar{w}_{j-\frac{1}{2}}^{n+1} + a_{j+\frac{1}{2}}^n \bar{w}_{j+\frac{1}{2}}^{n+1}) + \frac{1}{\Delta t}(\bar{w}_j^{n+1} - \bar{u}_j^n) - \frac{1}{\Delta x}(a_{j-\frac{1}{2}}^n + a_{j+\frac{1}{2}}^n)\bar{w}_j^{n+1} \right\}.$$

---

[1]The choice of symmetric intervals around $\tilde{I}_j$ yield methods of odd order. For methods of even order, it suffices to sacrifice one of the side constraints, $p = \pm\frac{r-1}{2}$.

As $\Delta t \downarrow 0$ we end up with limiting values which depend solely on the reconstructed values $R(x, u)$ on both sides of the interfacing breakpoints, $x_{j\pm\frac{1}{2}}$, given by

$$u(x^n_{j+\frac{1}{2},l}, t) \rightarrow p^n_j(x_{j+\frac{1}{2}}) =: u^-_{j+\frac{1}{2}}(t)$$

(2.16)

$$u(x^n_{j+\frac{1}{2},r}, t) \rightarrow p^n_{j+1}(x_{j+\frac{1}{2}}) =: u^+_{j+\frac{1}{2}}(t);$$

here $p^n_j(x)$ and $p^n_{j+1}(x)$ are the polynomial reconstructions of $R(x; \bar{u}^n)$ at the original time step t^n introduced in (2.3). The corresponding averages in (2.5) approach $\bar{w}^{n+1}_{j+\frac{1}{2}} \sim (\Delta f)_{j+\frac{1}{2}}/2a^n_{j+\frac{1}{2}}$ where $(\Delta f)_{j+\frac{1}{2}} := f(u^+_{j+\frac{1}{2}}) - f(u^-_{j+\frac{1}{2}})$, while the smoother averages in (2.6) are of order $\bar{w}^{n+1}_j \sim \bar{u}^n_j - \Delta t(\Delta f)_{j+\frac{1}{2}}$. Inserted into (2.15), we end up with a semi-discrete limit which can be written in its final conservative form,

(2.17)
$$\frac{d\bar{u}_j}{dt} = -\frac{H_{j+\frac{1}{2}}(t) - H_{j-\frac{1}{2}}(t)}{\Delta x};$$

here $H_{j\pm\frac{1}{2}}(t)$ are the numerical fluxes given by

(2.18)
$$H_{j+\frac{1}{2}}(t) := \frac{f(u^+_{j+\frac{1}{2}}(t)) + f(u^-_{j+\frac{1}{2}}(t))}{2} - \frac{a_{j+\frac{1}{2}}(t)}{2}\left[u^+_{j+\frac{1}{2}}(t) - u^-_{j+\frac{1}{2}}(t)\right].$$

Once again, we emphasize that among its several advantages, the versatility of this semi-discrete formulation is the independence of the specific reconstruction, (2.3), and evolution algorithms which are utilized to recover the interface values, $u^-_{j+\frac{1}{2}}$ and $u^+_{j+\frac{1}{2}}$ and to evolve the cell averages in (2.17). A description of our particular choices for these algorithms is provided in §3.

2.2. Two-dimensional Schemes. Starting with a general hyperbolic conservation law in two space dimensions,

(2.19)
$$u_t + f(u)_x + g(u)_z = 0,$$

we proceed as in §2.1, and consider the sliding averages of u over the cells $I_{j,k} := [x_{j-1/2}, x_{j+1/2}] \times [z_{k-1/2}, z_{k+1/2}]$,

$$\bar{u}^n_{j,k} := \fint_{I_{j,k}} u(x, z, t^n) \, dx \, dz,$$

where Δx and Δz represent the space scales in the x- and z-direction respectively.

As in the one-dimensional case, we seek a semi-discrete formulation for the evolution of the cell averages of the conservation law (2.19). We begin by incorporating the information provided by the local speeds of propagation, that we approximate by

(2.20) $\quad a^n_{j+\frac{1}{2},k} := \max\left\{\rho\left(\frac{\partial f}{\partial u}(u^W_{j+1,k})\right), \rho\left(\frac{\partial f}{\partial u}(u^E_{j,k})\right)\right\}, \quad b^n_{j,k+\frac{1}{2}} := \max\left\{\rho\left(\frac{\partial g}{\partial u}(u^S_{j,k+1})\right), \rho\left(\frac{\partial g}{\partial u}(u^N_{j,k})\right)\right\};$

where the cell interface values in the z- and x-direction,

(2.21)
$$u^N_{j,k} := p^n_{j,k}(x_j, z_{k+\frac{1}{2}}), \quad u^S_{j,k} := p^n_{j,k}(x_j, z_{k-\frac{1}{2}}),$$
$$u^E_{j,k} := p^n_{j,k}(x_{j+\frac{1}{2}}, z_k), \quad u^W_{j,k} := p^n_{j,k}(x_{j-\frac{1}{2}}, z_k)$$

are calculated via a non-oscillatory piecewise polynomial reconstruction,

(2.22)
$$R(x, z; \bar{u}^n) = \sum_{j,k} p^n_{j,k}(x, z)\mathbf{1}_{I_{j,k}};$$

the polynomials $\{p^n_{j,k}(x, z)\}$ are determined so that $R(x, z; \bar{u}^n)$ satisfies properties analogous to $\mathcal{P}_1 - \mathcal{P}_3$ above. This information allows us to separate between regions of smoothness, depicted as $D_{j,k}$ in Fig. 2.2, and regions of non-smoothness, depicted as the shaded regions. Nine sets of cell averages are calculated as follows:
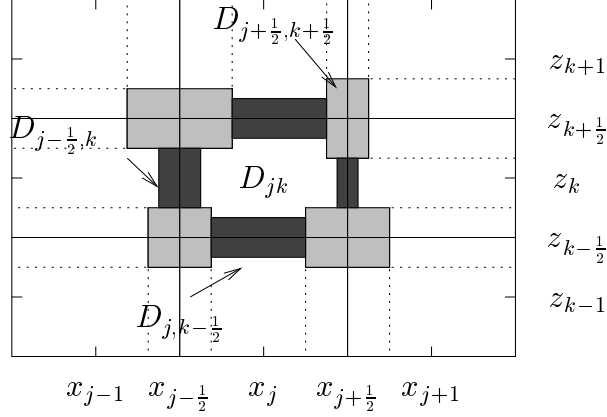
Fig. 2.2: Floor plan for modified central differencing in two-space dimensions.

- In the clear shaded regions, $D_{j\pm\frac{1}{2},k\pm\frac{1}{2}}$, the solution is not smooth in both directions; staggered evolution over the control volumes $D_{j\pm\frac{1}{2},k\pm\frac{1}{2}} \times [t^n, t^{n+1}]$ is used to obtain the new cell averages $\{\bar{w}^{n+1}_{j\pm\frac{1}{2},k\pm\frac{1}{2}}\}$,
- In the dark shaded regions, $D_{j\pm\frac{1}{2},k}$ and $D_{j,k\pm\frac{1}{2}}$, the solution is smooth only in one direction; staggered evolution is used along the non-smooth interfaces to obtain, respectively, the cell averages $\{\bar{w}^{n+1}_{j\pm\frac{1}{2},k}\}$ and $\{\bar{w}^{n+1}_{j,k\pm\frac{1}{2}}\}$,
- To evolve the smooth part of the solution, we integrate the polynomial $p^n_{j,k}(x, z)$ and the corresponding fluxes over the non rectangular control volume $D_{j,k} \times [t^n, t^{n+1}]$; these cell averages are denoted by $\{\bar{w}^{n+1}_{j,k}\}$.

This approach allows us to form a new polynomial, denoted $R(x, z; \bar{w}^{n+1})$, which is reconstructed from these smooth and non-smooth portions of the solution, and to reproject it back onto the original grid-cells,

$$(2.23) \qquad \bar{u}^{n+1}_{j,k} = \fint_{I_{j,k}} R\left(x, z; \bar{w}^{n+1}\right) \, dx \, dz.$$

The resulting non-staggered fully-discrete scheme admits a more versatile semi-discrete limit as $\Delta t \to 0$,

$$(2.24) \qquad \frac{d}{dt}\bar{u}_{j,k}(t) = -\frac{H^x_{j+\frac{1}{2},k}(t) - H^x_{j-\frac{1}{2},k}(t)}{\Delta x} - \frac{H^z_{j,k+\frac{1}{2}}(t) - H^z_{j,k-\frac{1}{2}}(t)}{\Delta z},$$

with numerical fluxes

$$H^x_{j+\frac{1}{2},k}(t) = \frac{1}{12}\Big[f(u^{NW}_{j+1,k}(t)) + f(u^{NE}_{j,k}(t)) + 4(f(u^{W}_{j+1,k}(t)) + f(u^{E}_{j,k}(t))) + f(u^{SW}_{j+1,k}(t)) + f(u^{SE}_{j,k}(t))\Big]$$

$$(2.25) \qquad -\frac{a_{j+\frac{1}{2},k}(t)}{12}\Big(u^{NW}_{j+1,k}(t) - u^{NE}_{j,k}(t) + 4(u^{W}_{j+1,k}(t) - u^{E}_{j,k}(t)) + u^{SW}_{j+1,k}(t) - u^{SE}_{j,k}(t)\Big),$$

$$H^z_{j,k+\frac{1}{2}}(t) = \frac{1}{12}\Big[g(u^{SW}_{j,k+1}(t)) + g(u^{NW}_{j,k}(t)) + 4(g(u^{S}_{j,k+1}(t)) + g(u^{N}_{j,k}(t))) + g(u^{SE}_{j,k+1}(t)) + g(u^{NE}_{j,k}(t))\Big]$$

$$(2.26) \qquad -\frac{b_{j,k+\frac{1}{2}}(t)}{12}\Big(u^{SW}_{j,k+1}(t) - u^{NW}_{j,k}(t) + 4(u^{S}_{j,k+1}(t) - u^{N}_{j,k}(t)) + u^{SE}_{j,k+1}(t) - u^{NE}_{j,k}(t)\Big).$$

This particular version of the numerical fluxes results from using Simpson's quadrature rule to approximate the integrals of the fluxes f and g along the cell boundaries $[z_{k-\frac{1}{2}}, z_{k+\frac{1}{2}}]$ and $[x_{j-\frac{1}{2}}, x_{j+\frac{1}{2}}]$ respectively, and it incorporates information from the *corner* interface values,

$$(2.27) \qquad \begin{aligned} u^{NE}_{j,k} &:= \hat{p}^n_{j,k}(x_{j+\frac{1}{2}}, z_{k+\frac{1}{2}}), \quad u^{SW}_{j,k} := \hat{p}^n_{j,k}(x_{j-\frac{1}{2}}, z_{k-\frac{1}{2}}), \\ u^{SE}_{j,k} &:= \hat{p}^n_{j,k}(x_{j+\frac{1}{2}}, z_{k-\frac{1}{2}}), \quad u^{NW}_{j,k} := \hat{p}^n_{j,k}(x_{j-\frac{1}{2}}, z_{k+\frac{1}{2}}), \end{aligned}$$

8

into the scheme. These corner values are recovered via the non-oscillatory reconstruction $\hat{R}(x,z;\bar{u}^n) = \sum \hat{p}^n_{j,k}(x,z) \cdot$ $\mathbf{1}_{I_{j,k}}$, which **may coincide with the original reconstruction**, $R(x,z;\bar{u}^n)$, or, alternatively, interpolate the cell values along the diagonal directions shown in figure 2.3(b) so as to prevent the onset of spurious oscillations along those axis.
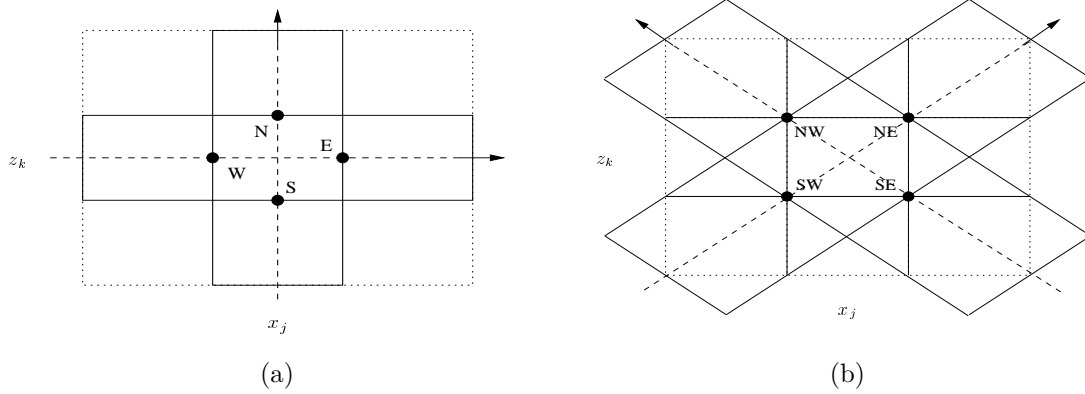

Fig. 2.3: (a) reconstruction in x- and z- directions. (b) diagonal axis for reconstruction.

3. Implementation of Semi-discrete Central Schemes. The framework of semi-discrete scheme described above entertains a wide range of options for the implementation of their two main ingredients: non-oscillatory reconstruction and evolution. In this section we provide some examples of non-oscillatory reconstructions and evolution routines that we implemented for computing the solutions of the system (1.1) – (1.4) presented in §4 and §5 below.

3.1. Third-order CWENO Reconstruction. Our first choice for the reconstruction of the point values of u is the third-order CWENO polynomial reconstruction of Kurganov and Levy, [12]. A piecewise quadratic polynomial that satisfies the essential properties $\mathcal{P}_1$, $\mathcal{P}_2$, and $\mathcal{P}_3$ above is formed as follows: in each cell $I_j = [x_{j-\frac{1}{2}}, x_{j+\frac{1}{2}}]$, the polynomials $\{p^n_j(x)\}$ in (2.3) are written as a convex combination of three polynomials $P_L(x)$, $P_C(x)$, and $P_R(x)$,

$$(3.1) \qquad p^n_j(x) = w_L P_L(x) + w_C P_C(x) + w_R P_R(x), \quad \sum_{i \in \{L,C,R\}} w_i = 1,$$

where the linear polynomials

$$(3.2) \qquad P_L(x) = \bar{u}^n_j + \frac{\bar{u}^n_j - \bar{u}^n_{j-1}}{\Delta x}(x - x_j), \quad \text{and} \quad P_R(x) = \bar{u}^n_j + \frac{\bar{u}^n_{j+1} - \bar{u}^n_j}{\Delta x}(x - x_j),$$

conserve the pair of cell averages $\bar{u}^n_{j-1}$, $\bar{u}^n_j$ and $\bar{u}^n_j$, $\bar{u}^n_{j+1}$ respectively, and the parabola centered around x_j,

$$(3.3) \qquad P_C(x) = \bar{u}^n_j - \frac{1}{12}(\bar{u}^n_{j-1} - 2\bar{u}^n_j + \bar{u}^n_{j+1})$$
$$+ \frac{\bar{u}^n_{j+1} - \bar{u}^n_{j-1}}{2\Delta x}(x - x_j) + \frac{\bar{u}^n_{j-1} - 2\bar{u}^n_j + \bar{u}^n_{j+1}}{\Delta x^2}(x - x_j)^2,$$

is determined so as to satisfy

$$c_L P_L(x) + c_R P_R(x) + (1 - c_L - c_R)P_C(x) = u^n_j + u'_j(x - x_j) + \frac{1}{2}u''_j(x - x_j)^2,$$

9

where u_j^n, u_j' and u_j'' approximate the point values $u(x_j, t^n)$, $u_x(x_j, t^n)$, and $u_{xx}(x_j, t^n)$ given respectively by

$$u_j^n := \bar{u}_j^n - \frac{1}{24}(\bar{u}_{j-1}^n - 2\bar{u}_j^n + \bar{u}_{j+1}^n),$$

(3.4)
$$u_j' := \frac{\bar{u}_{j+1}^n - \bar{u}_{j-1}^n}{2\Delta x}, \quad \text{and} \quad u_j'' := \frac{\bar{u}_{j-1}^n - 2\bar{u}_j^n + \bar{u}_{j+1}^n}{\Delta x^2}.$$

We guarantee the conservation of the cell averages $\bar{u}_{j-1}^n$, $\bar{u}_j^n$ and $\bar{u}_{j+1}^n$ by any symmetric choice of the weights c_i (e.g., $c_{\text{L}} = c_{\text{R}} = 1/4$, $c_{\text{C}} = 1/2$), and the accuracy property, $\mathcal{P}_2$, in smooth regions, [17]

$$p_j^n(x) = u(x, t^n) + \mathcal{O}((\Delta x)^3), \quad x \in [x_{j-\frac{1}{2}}, x_{j+\frac{1}{2}}].$$

The non-oscillatory behavior of $\{p_j^n(x)\}$ –property $\mathcal{P}_3$, is attained with the non-linear weights

(3.5)
$$w_i = \frac{\alpha_i}{\sum_m \alpha_m}, \quad \text{with} \quad \alpha_i = \frac{c_i}{(\epsilon + IS_i)^2}, \quad i, m \in \{\text{L}, \text{C}, \text{R}\},$$

where $\epsilon \ll 1$ prevents the denominator from vanishing (for the calculations in §4 and §5 we choose $\epsilon = 10^{-6}$), and the smoothness indicators, IS_i, provide a local measure of the derivatives of $P_i(x)$,

(3.6)
$$IS_i = \sum_{l=1}^{2} \int_{I_j} (\Delta x)^{2l-1} (P_i^{(l)}(x))^2 dx, \quad i \in \{\text{L}, \text{C}, \text{R}\},$$

switching automatically to the second-order reconstructions P_{L} and P_{R} in the presence of steep gradients and avoiding the onset of spurious oscillations, [9, 12, 17]. In this case, they read

$$IS_{\text{L}} = (\bar{u}_j^n - \bar{u}_{j-1}^n)^2, \qquad IS_{\text{R}} = (\bar{u}_{j+1}^n - \bar{u}_j^n)^2,$$

(3.7)
$$IS_{\text{C}} = \frac{13}{3}(\bar{u}_{j+1}^n - 2\bar{u}_j^n + \bar{u}_{j-1}^n)^2 + \frac{1}{4}(\bar{u}_{j+1}^n - \bar{u}_{j-1}^n)^2.$$

Remarks:

1. For this particular reconstruction, the one-dimensional interface values, $u_{j+\frac{1}{2}}^-(t)$ and $u_{j+\frac{1}{2}}^+(t)$, required in the numerical flux (2.18) take the explicit form

$$u_{j+\frac{1}{2}}^-(t^n) := p_j^n(x_{j+\frac{1}{2}}) = \frac{1}{2}w_{\text{L}}(3\bar{u}_j^n - \bar{u}_{j-1}^n) + \frac{1}{12}w_{\text{C}}(-5\bar{u}_{j+1}^n + 8\bar{u}_j^n - \bar{u}_{j-1}^n) + \frac{1}{2}w_{\text{R}}(\bar{u}_{j+1}^n + \bar{u}_j^n),$$

$$u_{j+\frac{1}{2}}^+(t^n) := p_{j+1}^n(x_{j+\frac{1}{2}}) = \frac{1}{2}w_{\text{L}}(\bar{u}_{j+1}^n + \bar{u}_j^n) + \frac{1}{12}w_{\text{C}}(-\bar{u}_{j+2}^n + 8\bar{u}_{j+1}^n - 5\bar{u}_j^n) + \frac{1}{2}w_{\text{R}}(-\bar{u}_{j+2}^n + 3\bar{u}_{j+1}^n).$$

2. In the case of systems of equations, the choice of these smoothness indicators is, indeed, non-trivial. The different conserved quantities involved in any particular system (density, momentum, etc.) may very well develop discontinuities at different points throughout the solution domain that do not affect every other quantity in the system. Hence, choosing the smoothness indicators individually for each quantity may cause the scheme to use different stencils for different quantities during the same evolution step. This can be avoided by either using *global* smoothness indicators, e.g., an (norm-scaled) average of the individual ones, or by identifying those that are physically relevant, such as, e.g., the density near a contact discontinuity (see §4 for our particular choices in the one-dimensional case and [16] for an in-depth discussion about the selection of smoothness indicators for systems of equations).

In two- and higher- space dimensions, a possibility for calculating the interface values in (2.21) and (2.27) in a rather straight forward way is to apply this one-dimensional third-order reconstruction *dimension-by-dimension* in the x- and z- directions (Fig. 2.3 (a)), and, if so desired, in the two diagonal directions of the coordinate frame displayed in figure 2.3(b). In two dimensions, however, we note that the constant term in the *central*

10

parabola, (3.3), requires an additional correction (in the transverse direction of the reconstruction) in order to guarantee third-order accuracy when the point value $u(x_j, z_k, t^n)$ is recovered from the neighboring cell averages,

$$u(x_j, z_k, t^n) = \bar{u}^n_{j,k} - \frac{1}{12}(\bar{u}^n_{j-1,k} - 2\bar{u}^n_{j,k} + \bar{u}^n_{j+1,k}) - \frac{1}{12}(\bar{u}^n_{j,k-1} - 2\bar{u}^n_{j,k} + \bar{u}^n_{j,k+1}) + \mathcal{O}((\max\{\Delta x, \Delta z\})^3).$$

That is, along the line $z = z_k$, the reconstruction in the x-direction is carried out using the linear polynomials $P_{\mathrm{L}}(x, z_k)$ and $P_{\mathrm{R}}(x, z_k)$ as in (3.2), and the parabola $P_{\mathrm{C}}(x, z_k)$, given by

$$P_{\mathrm{C}}(x, z_k) = \bar{u}^n_{j,k} - \frac{1}{12}(\bar{u}^n_{j-1,k} - 2\bar{u}^n_{j,k} + \bar{u}^n_{j+1,k}) - \frac{1}{12}(\bar{u}^n_{j,k-1} - 2\bar{u}^n_{j,k} + \bar{u}^n_{j,k+1})$$

(3.8)
$$+ \frac{\bar{u}^n_{j+1,k} - \bar{u}^n_{j-1,k}}{2\Delta x}(x - x_j) + \frac{\bar{u}^n_{j-1,k} - 2\bar{u}^n_j + \bar{u}^n_{j+1,k}}{\Delta x^2}(x - x_j)^2.$$

The same reconstruction is carried out in the z-direction, holding $x = x_j$ fixed. And, should one choose to implement the reconstruction along the diagonal directions, the corresponding polynomials are given by (consult [13] for additional details)

(3.9)
$$\hat{p}^n_{j,k}(x, z) = \hat{w}_{\mathrm{L}} \hat{P}_{\mathrm{L}}(x, z) + \hat{w}_{\mathrm{C}} \hat{P}_{\mathrm{C}}(x, z) + \hat{w}_{\mathrm{R}} \hat{P}_{\mathrm{R}}(x, z),$$

with

$$\hat{P}_{\mathrm{L}}(x, z) = \bar{u}^n_{j,k} + \frac{\bar{u}^n_{j,k} - \bar{u}^n_{j-1,k-1}}{\Delta}\left(\frac{\Delta}{2\Delta z}(z - z_k) + \frac{\Delta}{2\Delta x}(x - x_j)\right)$$

$$\hat{P}_{\mathrm{C}}(x, z) = \bar{u}^n_{j,k} - \frac{1}{12}(\bar{u}^n_{j+1,k+1} - 2\bar{u}^n_{j,k} + \bar{u}^n_{j-1,k-1}) - \frac{1}{12}(\bar{u}^n_{j-1,k+1} - 2\bar{u}^n_{j,k} + \bar{u}^n_{j+1,k-1})$$

$$+ \frac{\bar{u}^n_{j+1,k+1} - \bar{u}^n_{j-1,k-1}}{2\Delta}\left(\frac{\Delta}{2\Delta z}(z - z_k) + \frac{\Delta}{2\Delta x}(x - x_j)\right)$$

$$+ \frac{\bar{u}^n_{j+1,k+1} - 2\bar{u}^n_{j,k} + \bar{u}^n_{j-1,k-1}}{\Delta^2}\left(\frac{\Delta}{2\Delta z}(z - z_k) + \frac{\Delta}{2\Delta x}(x - x_j)\right)^2$$

(3.10) $$\hat{P}_{\mathrm{R}}(x, z) = \bar{u}^n_{j,k} + \frac{\bar{u}^n_{j+1,k+1} - \bar{u}^n_{j,k}}{\Delta}\left(\frac{\Delta}{2\Delta z}(z - z_k) + \frac{\Delta}{2\Delta x}(x - x_j)\right),$$

along the SW–NE axis, and

$$\hat{P}_{\mathrm{L}}(x, z) = \bar{u}^n_{j,k} + \frac{\bar{u}^n_{j,k} - \bar{u}^n_{j+1,k-1}}{\Delta}\left(\frac{\Delta}{2\Delta z}(z - z_k) - \frac{\Delta}{2\Delta x}(x - x_j)\right)$$

$$\hat{P}_{\mathrm{C}}(x, z) = \bar{u}^n_{j,k} - \frac{1}{12}(\bar{u}^n_{j+1,k+1} - 2\bar{u}^n_{j,k} + \bar{u}^n_{j-1,k-1}) - \frac{1}{12}(\bar{u}^n_{j-1,k+1} - 2\bar{u}^n_{j,k} + \bar{u}^n_{j+1,k-1})$$

$$+ \frac{\bar{u}^n_{j-1,k+1} - \bar{u}^n_{j+1,k-1}}{2\Delta}\left(\frac{\Delta}{2\Delta z}(z - z_k) - \frac{\Delta}{2\Delta x}(x - x_j)\right)$$

$$+ \frac{\bar{u}^n_{j-1,k+1} - 2\bar{u}^n_{j,k} + \bar{u}^n_{j+1,k-1}}{\Delta^2}\left(\frac{\Delta}{2\Delta z}(z - z_k) - \frac{\Delta}{2\Delta x}(x - x_j)\right)^2$$

(3.11) $$\hat{P}_{\mathrm{R}}(x, z) = \bar{u}^n_{j,k} + \frac{\bar{u}^n_{j+1,k+1} - \bar{u}^n_{j,k}}{\Delta}\left(\frac{\Delta}{2\Delta z}(z - z_k) - \frac{\Delta}{2\Delta x}(x - x_j)\right),$$

along the SE–NW axis where $\Delta = \sqrt{(\Delta x)^2 + (\Delta z)^2}$. The non-linear weights, $\hat{w}_i$, are also calculated direction by direction according to the one-dimensional recipe (3.5) with the smoothness indicators given by the *norm-scaled* average of the componentwise indicators, $IS_i^{(m)}$, calculated as in (3.7),

(3.12)
$$IS_i = \frac{1}{d}\sum_{m=1}^{d}\frac{1}{\|u^{(m)}\|_2 + \epsilon} IS_i^{(m)}, \quad i \in \{\mathrm{L}, \mathrm{C}, \mathrm{R}\},$$

11

where $u^{(m)}$ stands for the mth component of u, and $\|u^{(m)}\|_2^2 = \sum_{j,k} |u_{j,k}^{(m)}|^2 \Delta x \Delta z$ represents its ℓ_2 norm over the discretized solution domain.

3.2. CWENO Fourth-order Reconstruction. In §5 below we demonstrate the versatility of the central semi-discrete scheme (2.24)–(2.26) by implementing the dimension-by-dimension third-order reconstruction described above and the *genuinely multi-dimensional* fourth-order CWENO reconstruction of Levy et. al., [18, 1], that recovers the interface point values in (2.21) and (2.27) via a bi-quadratic polynomial interpolant satisfying the desired conservation, accuracy and non-oscillatory properties in two-space dimensions. Following is an outline of this fourth-order reconstruction, originally developed by Levy et. al. within the central, fully-discrete, staggered framework. In each cell $I_{j,k}$, the piecewise polynomial interpolants in (2.22), $p_{j,k}^n(x, z)$, are written as a convex combination of nine bi-quadratic polynomials, $P_{j+p,k+q}(x, z)$, that conserve the cell averages $\{\bar{u}_{j+p,k+q}^n\}_{p,q=-1}^1$ and approximate the pointvalues of $u(x, z, t^n)$ within fourth-order accuracy,

$$(3.13) \qquad p_{j,k}^n(x, z) = \sum_{p,q=-1}^{1} w_{j,k}^{p,q} P_{j+p,k+q}(x, z), \quad \sum_{p,q=-1}^{1} w_{j,k}^{p,q} = 1, \;\; w_{j,k}^{p,q} \geq 0;$$

where the polynomials $P_{j,k}(x, z)$ have the form (omitting, for simplicity, the j and k indeces in the coefficients $\{b_m\}$),

$$
\begin{aligned}
P_{j,k}^n(x, z) = b_0 + {}& b_1(x - x_j) + b_2(z - z_k) + b_3(x - x_j)(z - z_k) \\
& + b_4(x - x_j)^2 + b_5(z - z_k)^2 + b_6(x - x_j)^2(z - z_k) \\
& + b_7(x - x_j)(z - z_k)^2 + b_8(x - x_j)^2(z - z_k)^2.
\end{aligned}
$$
$$(3.14)$$

The nine conservation constraints,

$$(3.15) \qquad \int_{x_{j-\frac{1}{2}}+p\Delta x}^{x_{j+\frac{1}{2}}+p\Delta x} \int_{z_{k-\frac{1}{2}}+q\Delta z}^{z_{k+\frac{1}{2}}+q\Delta z} P_{j,k}(x, z)dz \; dx = \bar{u}_{j+p,k+q}^n, \quad p, q = -1, 0, 1,$$

uniquely determine the 9 coefficients $\{b_m\}$,

$$
\begin{aligned}
b_0 &= \bar{u}^n - \frac{\Delta x^2}{24}\hat{u}_{xx} - \frac{\Delta z^2}{24}\hat{u}_{zz} + \frac{\Delta x^2 \Delta z^2}{24^2}\hat{u}_{xxzz}, \\
b_1 &= \hat{u}_x - \frac{\Delta z^2}{24}\hat{u}_{xzz}, & b_2 &= \hat{u}_z - \frac{\Delta x^2}{24}\hat{u}_{xxz}, \\
b_3 &= \hat{u}_{xz}, & b_4 &= \frac{1}{2}\hat{u}_{xx} - \frac{\Delta z^2}{48}\hat{u}_{xxzz}, \\
b_5 &= \frac{1}{2}\hat{u}_{zz} - \frac{\Delta x^2}{48}\hat{u}_{xxzz}, & b_6 &= \frac{1}{2}\hat{u}_{xxz}, \\
b_7 &= \frac{1}{2}\hat{u}_{xzz}, & b_8 &= \frac{1}{4}\hat{u}_{xxzz};
\end{aligned}
$$

12

where the divided differences

$$\hat{u}_{x_{j,k}} = \frac{\bar{u}^n_{j+1,k} - \bar{u}^n_{j-1,k}}{2\Delta x}, \qquad \hat{u}_{z_{j,k}} = \frac{\bar{u}^n_{j,k+1} - \bar{u}^n_{j,k-1}}{2\Delta z},$$

$$\hat{u}_{xx_{j,k}} = \frac{\bar{u}^n_{j+1,k} - 2\bar{u}^n_{j,k} + \bar{u}^n_{j-1,k}}{\Delta x^2}, \qquad \hat{u}_{zz_{j,k}} = \frac{\bar{u}^n_{j,k+1} - 2\bar{u}^n_{j,k} + \bar{u}^n_{j,k-1}}{\Delta z^2},$$

$$\hat{u}_{xz_{j,k}} = \frac{\bar{u}^n_{j+1,k+1} - \bar{u}^n_{j+1,k-1} - \bar{u}^n_{j-1,k+1} + \bar{u}^n_{j-1,k-1}}{4\Delta x\Delta z},$$

$$\hat{u}_{xxz_{j,k}} = \frac{(\bar{u}^n_{j+1,k+1} - 2\bar{u}^n_{j,k+1} + \bar{u}^n_{j-1,k+1}) - (\bar{u}^n_{j+1,k-1} - 2\bar{u}^n_{j,k-1} + \bar{u}^n_{j-1,k-1})}{2\Delta x^2\Delta z},$$

$$\hat{u}_{xzz_{j,k}} = \frac{(\bar{u}^n_{j+1,k+1} - 2\bar{u}^n_{j+1,k} + \bar{u}^n_{j+1,k-1}) - (\bar{u}^n_{j-1,k+1} - 2\bar{u}^n_{j-1,k} + \bar{u}^n_{j-1,k-1})}{2\Delta x\Delta z^2},$$

$$\hat{u}_{xxzz_{j,k}} = \frac{1}{\Delta x^2\Delta z^2}\big[(\bar{u}^n_{j+1,k+1} - 2\bar{u}^n_{j+1,k} + \bar{u}^n_{j+1,k-1}) - 2(\bar{u}^n_{j,k+1} - 2\bar{u}^n_{j,k} + \bar{u}^n_{j,k-1})$$
$$+ (\bar{u}^n_{j-1,k+1} - 2\bar{u}^n_{j-1,k} + \bar{u}^n_{j-1,k-1})\big],$$

serve to approximate the values of u and its partial derivatives at the points (x_j, z_k) within the fourth-order accuracy constraints of the method.

As in the third-order reconstruction, the non-linear weights in (3.13), $w^{p,q}_{l,k}$, are computed so as to provide maximum accuracy in smooth regions and prevent oscillations in the non-smooth regions by eliminating the contribution of polynomials with steep gradients across the cell interfaces. For each cell nine weights are calculated,

(3.16) $$w^{p,q}_{j,k} = \frac{\alpha^{p,q}_{j,k}}{\sum_{m,n}\alpha^{m,n}_{j,k}}, \quad \text{with} \quad \alpha^{p,q}_{j,k} = \frac{c^{p,q}_{j,k}}{(\epsilon + IS^{p,q}_{j,k})^2}, \quad m,n,p,q = -1,0,1,$$

and the linear coefficients, $c^{p,q}_{j,k}$, chosen so that symmetry guarantees fourth-order accuracy,

$$c^{0,0}_{j,k} = \frac{1}{2} \qquad \text{and} \qquad c^{p,q}_{j,k} = \frac{1}{16}, \quad \forall\, p,q \neq 0;$$

convexity, $\sum_{p,q=-1}^{1} c^{p,q}_{j,k} = 1$, $c^{p,q}_{j,k} \geq 0$, guarantees conservation.

Global smoothness indicators are chosen according to (3.12). Unlike the third-order reconstruction where the exact calculation of the individual smoothness indicators is trivial and renders simple formulas, i.e., (3.7), in this fourth-order case, the exact calculation of the local L^2-norm of the partial derivatives of the polynomials $P^{p,q}_{j,k}$ is impractical. Instead, a Gaussian quadrature formula is used to approximate the integrals

$$IS^{p,q}_{j,k} = \int_{I_{j,k}} (|\partial_x P_{j+p,k+q}|^2 + |\partial_z P_{j+p,k+q}|^2 + (\Delta x)^2|\partial_{xx} P_{j+p,k+q}|^2 + (\Delta z)^2|\partial_{zz} P_{j+p,k+q}|^2)\, dx\, dz.$$

This approach still serves the purpose of automatically detecting and re-directing the numerical stencils in the direction of smoothness, thus preventing the onset of oscillations, [18].

3.3. Time Evolution: SSP Runge-Kutta Solvers. With the interface values (2.16), (2.21), and (2.27) computed with either one of the above CWENO reconstructions, we denote, for any grid function $w = \{w_j(t)\}$, the numerical fluxes on the right of (2.17) and (2.24) by

(3.17) $$C[w(t)] = -\frac{H_{j+\frac{1}{2}}(w(t)) - H_{j-\frac{1}{2}}(w(t))}{\Delta x}$$

13

and

$$(3.18) \qquad C[w(t)] = -\frac{H^x_{j+\frac{1}{2},k}(w(t)) - H^x_{j-\frac{1}{2},k}(w(t))}{\Delta x} - \frac{H^z_{j,k+\frac{1}{2}}(w(t)) - H^z_{j,k-\frac{1}{2}}(w(t))}{\Delta z},$$

respectively, and evolve the solution $u^{(0)} := \bar{u}^n_j$ from t^n, to t^{n+1} with an appropriate ODE solver. For the numerical calculations reported in §4 and §5, we choose the Strong Stability-preserving (SSP) Runge-Kutta discretizations [23, 5]. In particular, for the third-order results, we employ

$$
\begin{aligned}
u^{(1)} &= u^{(0)} + \Delta t C[u^{(0)}], \\
u^{(2)} &= u^{(1)} + \frac{\Delta t}{4}(-3C[u^{(0)}] + C[u^{(1)}]), \\
u^{n+1} := u^{(3)} &= u^{(2)} + \frac{\Delta t}{12}(-C[u^{(0)}] - C[u^{(1)}] + 8\ C[u^{(2)}]).
\end{aligned}
$$

(3.19)

and for the fourth-order results of §5.3

$$
\begin{aligned}
u^{(1)} &= u^{(0)} + \frac{\Delta t}{2}C[u^{(0)}], \\
u^{(2)} &= u^{(1)} + \frac{\Delta t}{2}(-C[u^{(0)}] + C[u^{(1)}]), \\
u^{(3)} &= u^{(2)} + \frac{\Delta t}{2}(-C[u^{(1)}] + 2\ C[u^{(2)}]), \\
u^{n+1} := u^{(4)} &= u^{(3)} + \frac{\Delta t}{6}(C[u^{(0)}] + 2C[u^{(1)}] - 4C[u^{(2)}] + C[u^{(3)}])
\end{aligned}
$$

(3.20)

is used to evolve the values reconstructed via the fourth-order CWENO interpolation algorithm of Levy et. al. of §3.2.

4. One-dimensional Numerical Results. In one space dimension, equations (1.1)–(1.4) admit the conservative form (2.1) with

$$(4.1) \qquad u = (\rho, \rho v_x, \rho v_y, \rho v_z, B_y, B_z, e)^\top,$$

$$f(u) = (\rho v_x, \rho v_x^2 + p^* - B_x^2, \rho v_x v_y - B_x B_y, \rho v_x v_z - B_x B_z, B_y v_x - B_x v_y,$$

$$(4.2) \qquad B_z v_x - B_x v_z, (e + p^*)v_x - B_x(B_x v_x + B_y v_y + B_z v_z))^\top,$$

where $p^* = p + \frac{1}{2}B^2$ stands for the total pressure (static plus magnetic).

In this section we present numerical simulations of this one-dimensional MHD equations, (2.1)–(4.2). The results were obtained using the semi-discrete central scheme (2.17)–(2.18) with the pointvalues $u^+_{j+\frac{1}{2}}(t)$ and $u^-_{j+\frac{1}{2}}(t)$, (2.16), computed via the CWENO third-order reconstruction of §3.1, and evolved according to Shu's third-order SSP Runge-Kutta scheme as outlined in §3.3. The schemes are implemented for computing the approximate solution of two coplanar shock tube MHD models described by Brio and Wu in [3]. We use a uniform grid in the space discretization, and in both cases we choose the time step dynamically with CFL restriction

$$(4.3) \qquad \Delta t = \frac{0.9\ \Delta x}{\max_k |a_k(u)|},$$

where $\{a_k(u)\}_k$ are the eigenvalues of the Jacobian matrix of $f(u)$.

14

4.1. Brio–Wu Shock Tube Problem. The first one-dimensional Riemann problem we consider consists of a shock tube with two initial equilibrium states, u_l and u_r, given by

$$(4.4) \qquad (\rho, v_x, v_y, v_z, B_y, B_z, p)^\top = \begin{cases} (1.0, 0, 0, 0, 1.0, 0, 1.0)^\top & \text{for } x < 0, \\ (0.125, 0, 0, 0, -1.0, 0, 0.1)^\top & \text{for } x > 0, \end{cases}$$

and complemented with the constant values of $B_x \equiv 0.75$ and $\gamma = 2$. The problem is solved for $x \in [-1, 1]$ with 800 grid points, and numerical results are presented at $t = 0.2$. Figure 4.1 show the density, the $x-$ and $y-$velocity components, the $y-$magnetic field, and pressure profiles. The hydrodynamical data of this problem is the same as that in Sod's shock tube problem of gas dynamics. The variety of MHD waves, however, poses a considerable challenge for high-resolution such as the *black-box* central schemes described in this paper. The solution of this problem consists of a left–moving fast rarefaction wave (FR), a slow compound wave (SM) which results from an intermediate shock that changes B_y from 0.58 to -0.31 and a slow rarefaction that changes B_y from -0.31 -0.53, a contact discontinuity (C), a right–moving slow shock (SS), and a right–moving fast rarefaction wave (FR). Note that the solution to this problem is not unique if B_z and v_z are not identically zero. The results in figure 4.1 are in agreement with those previously reported in [2], and are comparable with the second order upwind computations of Brio and Wu in [3], and with the fifth order WENO computations presented by Jiang and Wu in [11]. In fact, the present results show a better control of the oscillations that typically appear at the trailing edge of the right-moving fast rarefaction wave when high resolution schemes are employed. This better better control is due to our choice of smoothness indicators. Our various numerical experiments show that –in the absence of characteristic information– the average of the smoothness indicators of the density, ρ, and transverse magnetic field, B_y, (scaled by their ℓ_2 norm) is the best combination for selecting a single stencil for reconstruction and evolution of all the conserved quantities in the system. Our numerical results confirm the ability of central schemes, whether in their fully-discrete or semi-discrete formulations, to capture the main features of the discontinuous MHD solutions, while avoiding any characteristic information other than an estimate of the maximal speed of propagation, $\max_k |a_k(u)|$.

4.2. Brio–Wu High Mach Shock Tube Problem. The following shock tube model proposed by Brio and Wu in [3], is commonly used to check the robustness of the numerical schemes for high Mach number problems. The initial equilibrium states, u_l and u_r, are given by

$$(4.5) \qquad (\rho, v_x, v_y, v_z, B_y, B_z, p)^\top = \begin{cases} (1.0, 0, 0, 0, 1.0, 0, 1000)^\top & \text{for } x < 0, \\ (0.125, 0, 0, 0, -1.0, 0, 0.1)^\top & \text{for } x > 0, \end{cases}$$

and complemented with the values of $B_x \equiv 0$, and $\gamma = 2$. The Mach number of the right–moving shock wave is 15.5. If the plasma pressure is replaced by the sum of the static and magnetic pressures–denoted by p^* above, this model becomes a standard hydrodynamical Riemann problem. The solution is presented at $t = .012$, $x \in [-1, 1]$, with 200 grid points and with CFL number 0.9, consult (4.3).

The solution of this second Riemann problem consists of a left–moving fast rarefaction wave (FR), followed by a tangential discontinuity (TD), and a right moving fast shock (FS) with Mach number 15.5. Across the tangential discontinuity, the density, the magnetic field and the pressure can change, but both, the fluid velocity and the total pressure, $p + \frac{B^2}{2}$ are continuous.

As in the previous problem, our results are comparable to those reported in [2], [3], and [11] with second-order central and second- and fifth-order upwind scheme, and demonstrate the robustness of the schemes described in §2.
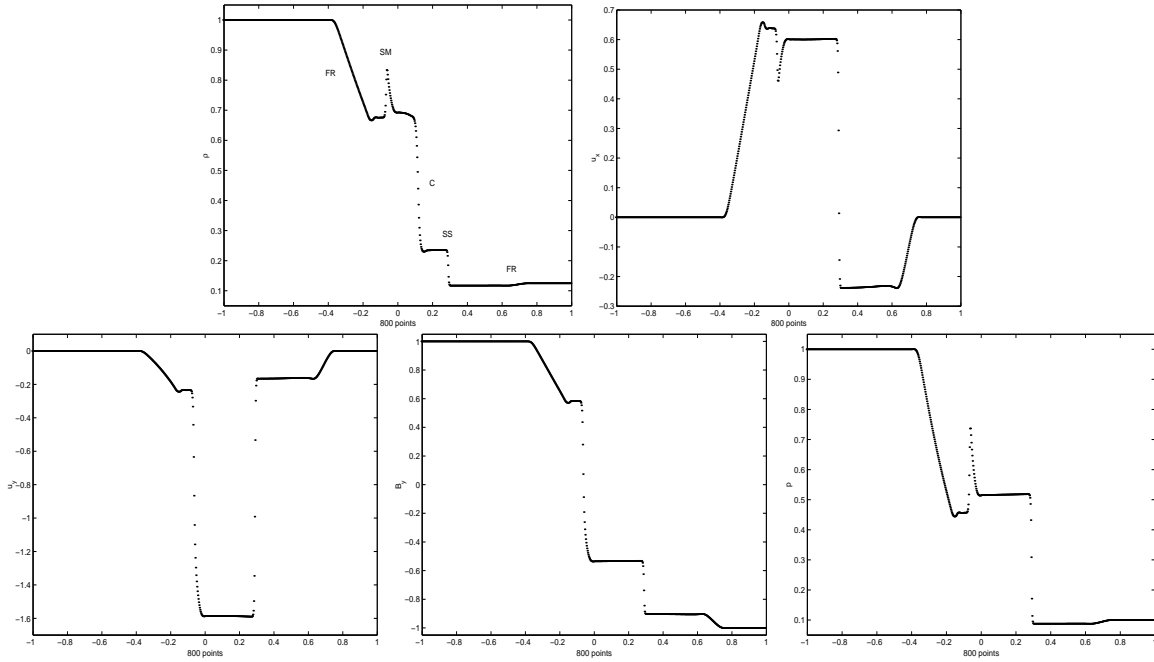
Fig. 4.1: Results of Brio-Wu shock tube problem at $t = 0.2$ computed with 800 grid points using third-order CWENO reconstruction, (3.1), and Shu's SSP Runge-Kutta solver, (3.19).
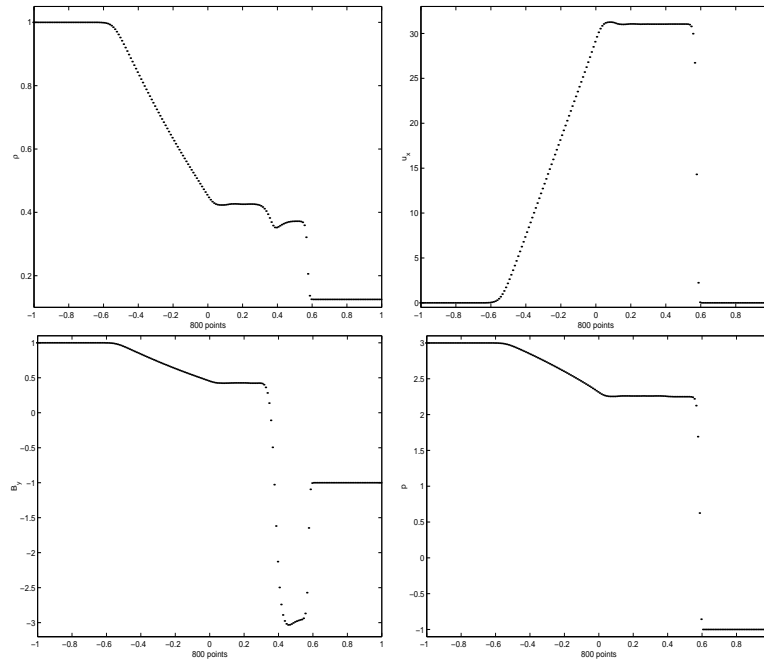

Fig. 4.2: Results of Brio-Wu high Mach problem at $t = 0.012$ computed with 200 grid points using third-order CWENO reconstruction, (3.1), and Shu's SSP Runge-Kutta solver, (3.19).

5. Two Dimensional Numerical Results. In two space dimensions, equations (1.1)–(1.4) admit the conservative form (2.19) with

(5.1)
$$u = (\rho, \rho v_x, \rho v_y, \rho v_z, B_x, B_y, B_z, e)^\top,$$

$$f(u) = (\rho v_x, \rho v_x^2 + p^* - B_x^2, \rho v_x v_y - B_x B_y, \rho v_x v_z - B_x B_z, 0, B_y v_x - B_x v_y,$$

(5.2)
$$B_z v_x - B_x v_z, (e + p^*)v_x - B_x(B_x v_x + B_y v_y + B_z v_z))^\top,$$

$$g(u) = (\rho v_z, \rho v_z v_x - B_z B_x, \rho v_z v_y - B_z B_y, \rho v_z^2 + p^* - B_z^2, B_x v_z - B_z v_x,$$

(5.3)
$$B_y v_z - B_z v_y, 0, (e + p^*)v_z - B_z(B_x v_x + B_y v_y + B_z v_z))^\top.$$

In this section we present the solution of four prototype problems for two–dimensional MHD equations. We begin testing our two–dimensional numerical schemes by solving the one–dimensional Brio–Wu shock tube problem described in §4.1 on a two–dimensional domain with the flow rotated 45°. For the second problem —the Kelvin–Helmholtz instability with transverse magnetic field configuration, we consider two different sets of boundary conditions in the $x-$direction: periodic in the first case and a free outflow boundary in the second convective setup. The third problem was introduced by Orszag and Tang in [21] as a simple model to study MHD turbulence. The last problem that we present simulates the interaction between a strong shock and a high-density cloud. These four problems appear extensively in the literature as they have become –in the absence of a rigorous stability condition for numerical schemes for MHD equations– standard tests to validate numerical algorithms. In all cases, the time scale, Δt is determined dynamically according to the CFL restriction

(5.4)
$$\Delta t = \frac{c}{\sqrt{(\max_k |a_k(u)|/\Delta x)^2 + (\max_k |b_k(u)|/\Delta z)^2}},$$

where $c < 1$ is a positive constant, and $\{a_k(u)\}_k$ and $\{b_k(u)\}_k$ represent the eigenvalues of the Jacobian matrices of $f(u)$ and $g(u)$ respectively.

It should be emphasized that the results presented below were obtained with the original formulation of semi-discrete central schemes in §2, namely, they were implemented "as is", *without* any enforcement of the solenoidal constraint (1.5). The $\nabla \cdot \mathbf{B} = 0$-constraint was *automatically* preserved to machine round-off error. In fact, the same test problems displayed below were first solved using the (global) projection method as a way to enforce the $\nabla \cdot \mathbf{B} = 0$-constraint. We observed that the divergence-free results displayed below avoid undesirable effects such as loss of conservation and monotonicity, often induced by global projection solvers.

5.1. Brio–Wu Rotated Flow. The initial conditions described by (4.4) are extended to the two–dimensional domain $[-1, 1] \times [-1, 1]$ and rotated 45° so that the fluid does not flow in the direction of the grid axis. Our results are displayed on figure 5.1, and they confirm the ability of central schemes to simulate discontinuous flows independently of the mesh orientation.
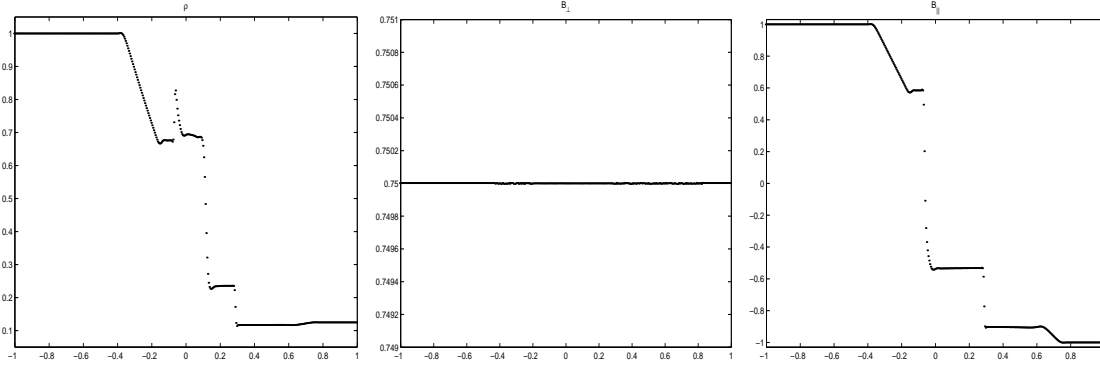
Fig. 5.1: Results of rotated Brio-Wu shock tube problem at $t = 0.2$ computed over a 600×600 mesh using third-order dimension-by-dimension CWENO reconstruction, (3.1), and Shu's SSP Runge-Kutta solver, (3.19). From left to right: density, transverse and parallel components of magnetic field (bottom)

We observe that the small deviations from the constant value of the transverse component of the magnetic that can be observed in figure 5.1 are well within the order of the scheme, and the numerical value of $\nabla \cdot \mathbf{B}$ is in the order of 10^{-13}.

5.2. Transverse Kelvin–Helmholtz Instability. The Kelvin–Helmholtz instability arises when two superposed fluids flow one over the other with a relative velocity. It models, for example, the important mechanism for the momentum transfer at the Earth's magnetopause boundary, which separates the solar wind from the Earth's magnetosphere, [11]. We approximate the solution of he two dimensional periodic and convective models with transverse magnetic field configuration with the semi-discrete scheme of Kurganov and Tadmor, (2.24)–(2.26), implemented along with the reconstruction of §3.1 and the SSP Runge-Kutta solver (3.19).In both cases, the governing equations are (5.1)–(5.3) are subject to initial conditions

$$(5.5) \qquad (\rho, v_x, v_y, v_z, B_x, B_y, B_z, p)^\top = (1.0, v_{x0} + \tilde{v}_{x0}, 0, 0, 0, 1.0, 0, 0.5)^\top,$$

where

$$(5.6) \qquad v_{x0} = \frac{v_0}{2} \tanh\left(\frac{z}{a}\right), \quad \text{and}$$

$$(5.7) \qquad \tilde{v}_{x0} = \begin{cases} -\tilde{v}_0 \sin\left(\frac{2\pi x}{\lambda}\right) \frac{1}{1+z^2}, & \text{if } -\frac{\lambda}{2} < x < \frac{\lambda}{2} \\ 0, & \text{otherwise}, \end{cases}$$

with $v_0 = 2$, $\tilde{v}_0 = -0.008$, $\lambda = 5\pi$ and $a = 1$. Also, the grids are stretched in the $z-$direction with a Roberts transformation, [11],

$$(5.8) \qquad z \leftarrow \frac{H \sinh\left(\tau z / 2H\right)}{\sinh\left(\tau / 2\right)}, \quad \tau = 6,$$

which renders a denser grid near $z = 0$ where the effect of the small initial perturbation $\tilde{v}_{x0}$ is more noticeable, and a coarser grid near $z = \pm H$, where little action takes place. The time step, Δt, is determined according to (5.4) with $c = 0.9$.
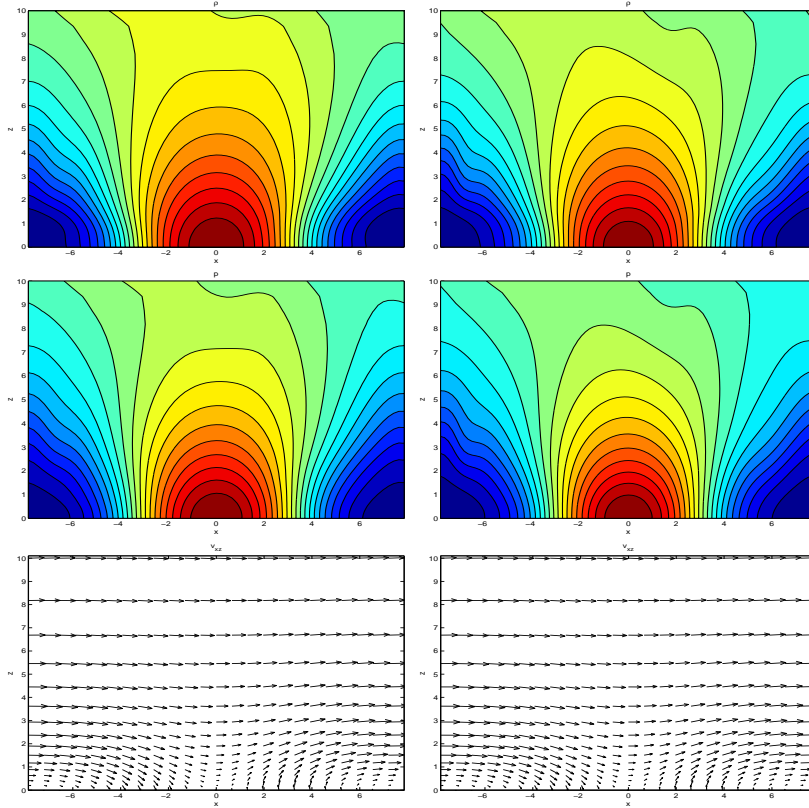
18

Fig. 5.2: Results of transverse Kelvin-Helmholtz instability with periodic $x-$boundary conditions computed with third order scheme. Left column uses 72×45 points and right column uses 96×60 grids respectively. There are 20 contours for density and pressure. Red–high value, blue–low value. Density ranges from 0.79 to 1.2, pressure range from 0.32 to 0.71 and maximum value for the velocity is 1.25.

In the periodic case, the computational domain is $[-\frac{L}{2}, \frac{L}{2}] \times [0, H]$, with $L = 5\pi$ and $H = 10$. The free outflow condition is applied at the top boundary, $z = H$, and the bottom boundary values are recovered by symmetry, since ρ, p, and B_y are symmetric, and v_x and v_z are antisymmetric under the transformation $(x, z) \rightarrow (-x, -z)$. In figure (5.2), we present solutions at $t = 144$, with 72×45 and 96×60 grid points. The resolution and accuracy of our results are comparable to those reported in [2] obtained, over two grids of sizes 96×96 and a 192×192 respectively, with the second-order staggered central scheme of Jiang and Tadmor; the gas kinetic scheme of Tang and Xu, [26], using a 200×200 uniform grid, and to those obtained with Jiang and Wu's fifth-order WENO scheme, [11], over two grids of sizes 48×30 and 96×60, respectively. The higher computational cost of the third-order reconstruction as compared to that of the fully-discrete second-order scheme we used in [2] is compensated by the fewer number of grid points needed to resolve accurately the steep gradients that characterize the solution.

In the convective setup, the initial conditions and perturbation are the same as in the periodic setup, (5.5)–(5.7). In this case, the free outflow condition is applied also in the x-direction over the computational domain $[-\frac{L}{2}, \frac{L}{2}] \times [0, H]$; where $H = 20$ and $L = 55\pi$, with $L >> \lambda$–so chosen to allow the excitation to convect freely without disturbing the $x-$boundaries. The values of the bottom boundary of the computational domain, $z = 0$, are recovered by symmetry as in the periodic configuration. Figures 5.3 and 5.4 display the solution over the region $[-50, 50] \times [-20, 20]$ computed with 792×92 grid points over computational domain at $t = 120$ and $t = 145$ respectively. The values of the bottom half of the solution domain are recovered using the same symmetry conditions as used to reconstruct the bottom boundary.
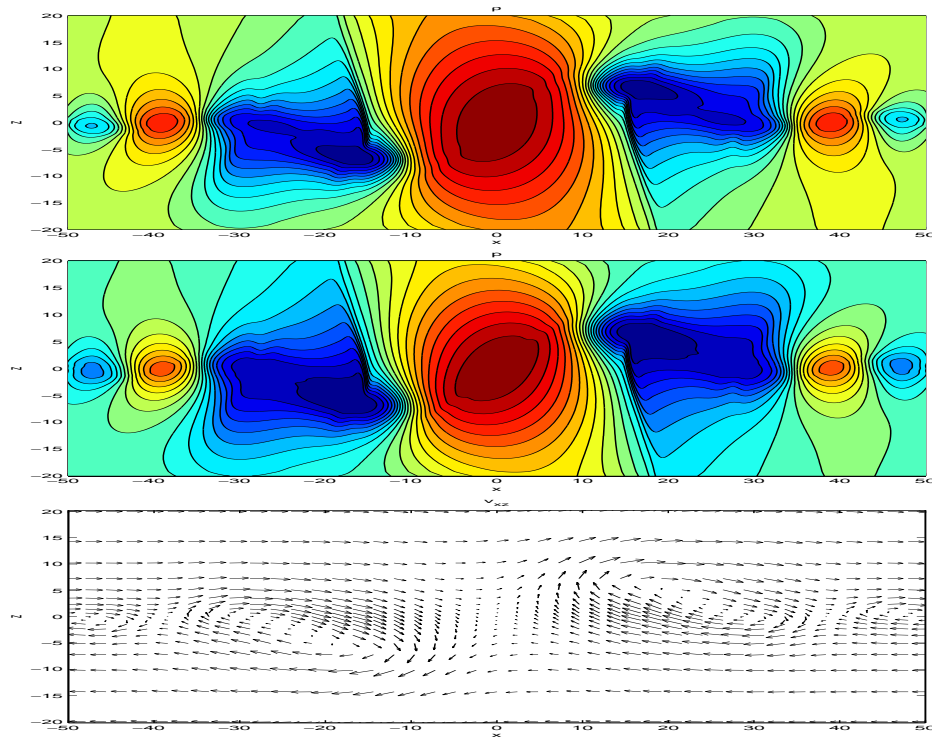
Fig. 5.3: Solution of convective Kelvin-Helmholtz instability at t=120, computed with third order scheme on a 792×72 grid, with $c = 0.9$. The density ranges from 0.63 to 1.3, and the pressure ranges from 0.20 to 0.85, the maximum value for the velocity is 1.54.
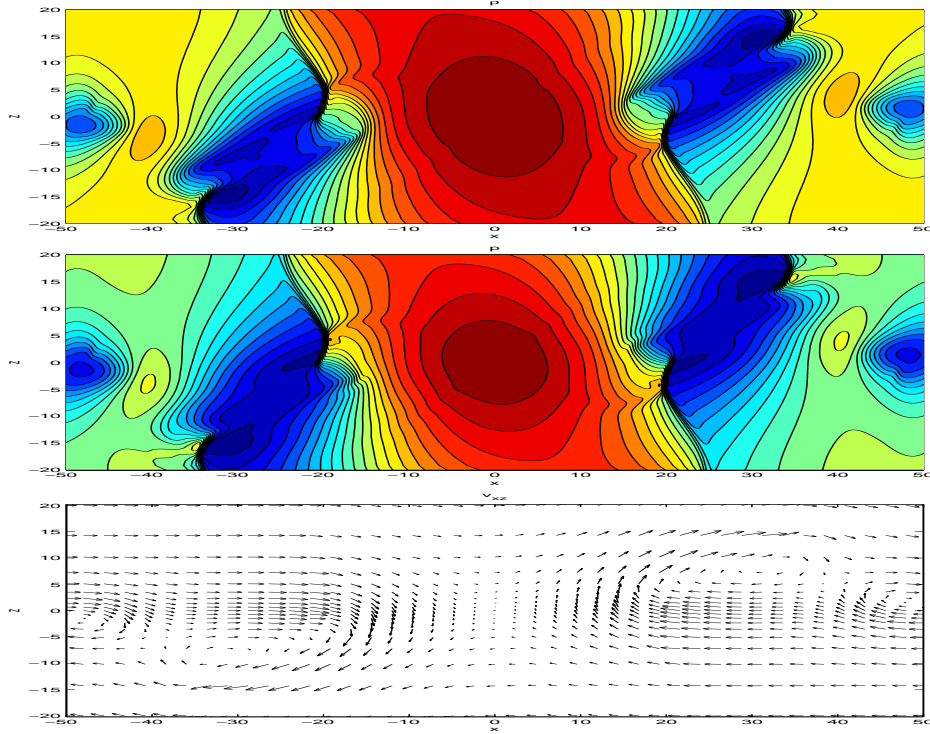
Fig. 5.4: Solution of convective Kelvin-Helmholtz instability at t=145, computed with third order scheme on a 792×72 grid. The Density ranges from 0.43 to 1.3, pressure ranges from 0.10 to 0.86 and maximum value for the velocity is 1.94.
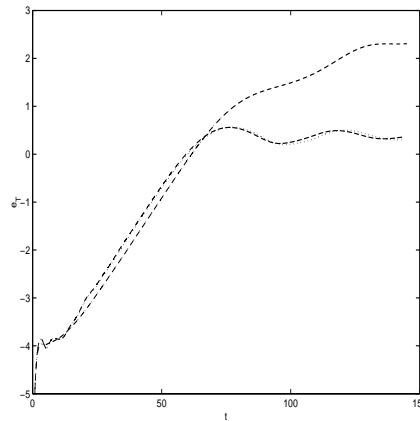

Fig. 5.5: Time evolution of the total transverse kinetic energy, $\log(\frac{1}{2} \int \rho v_z^2 dx dz)$, integrated over $[-L/2, L/2] \times [-H, H]$, for both periodic and convective Kelvin-Helmholtz instability. The results for the periodic case with 96×96 and 192×192 grid points are represented by a dashed and a doted curve respectively. The convective configuration is represented by a solid line.

5.3. Orszag–Tang MHD Turbulence Problem. This model considers the evolution of a compressible Orszag-Tang vortex system. The evolution of the vortex system involves the interaction between several shock waves traveling at various speed regimes [11, 28], which makes the problem useful to validate the robustness of

21

numerical schemes. The initial data is given by

$$\rho(x, z, 0) = \gamma^2, v_x(x, z, 0) = -\sin z, \, v_z(x, z, 0) = \sin x,$$
$$p(x, z, 0) = \gamma, B_x(x, z, 0) = -\sin z, B_z(x, z, 0) = \sin 2x$$

where $\gamma = 5/3$. With this data, the RMS values of the velocity and magnetic fields are both 1; the initial average Mach number is 1, and the average plasma beta is $10/3$. We solve the problem in $[0, 2\pi] \times [0, 2\pi]$, with periodic boundary conditions in both x- and z-directions. For this problem we implement the fourth-order reconstruction of §3.2 and the SSP Runge-Kutta fourth-order ODE solver (3.20) using a uniform grid with 192×192 points and $c = 0.9$ in (5.4).

Figures 5.6–5.8 below display the solution of the Orszag-Tang vortex system at $t = 0.5, t = 2$, and $t = 3$ respectively. These simulations were performed with 192×192 grid points using the fourth-order, genuinely multidimensional, CWENO reconstruction of §3.2 SSP Runge-Kutta solver (3.18)–(3.20). These results demonstrate the ability of higher-order central schemes to resolve the shocks that the vortex system develops while maintaining the simplicity and ease of implementation typical of this *black-box* type of finite-difference schemes. We also note that similar results were obtained with the dimension-by-dimension third-order reconstruction and the Runge-Kutta solver (3.19) using a 288×288 mesh. The improved resolution of the fourth-order scheme allows us to compute accurate approximations using coarser grids than those required by lower order schemes, thus reducing the computational cost of this type of simulations; an advantage that is more evident in higher space dimensions.
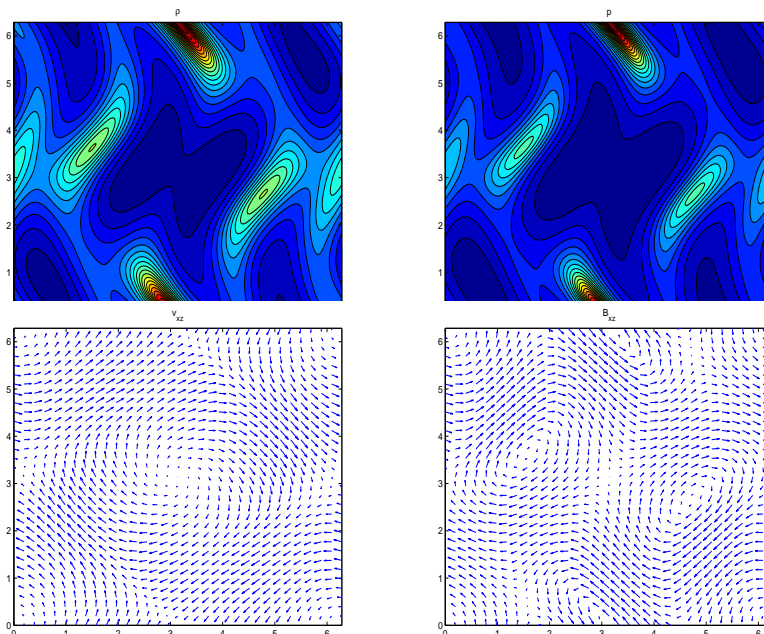

Fig. 5.6: Fourth-order solution of Orszag–Tang MHD turbulence problem with a 192×192 uniform grid at $t = 0.5$. There are 20 contours for density and pressure. Red –high value, blue –low value. Density range from 2.1 to 5.9, pressure range from 1.0 to 5.8. The maximum values of $|v|$ and $|B|$ are 1.6 and 1.6 respectively.
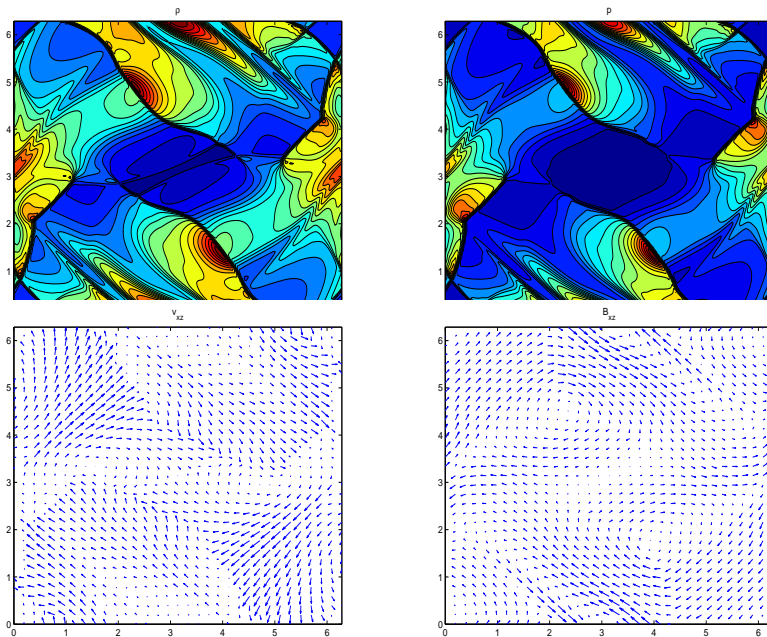
Fig. 5.7: Fourth-order solution of Orszag–Tang MHD turbulence problem with a 192×192 uniform grid at $t = 2$. There are 20 contours for density and pressure. Red–high value, blue–low value. Density ranges from 0.62 to 6.3, pressure ranges from 0.14 to 7.0. The maximum values of $|v|$ and $|B|$ are 1.6 and 2.8 respectively.
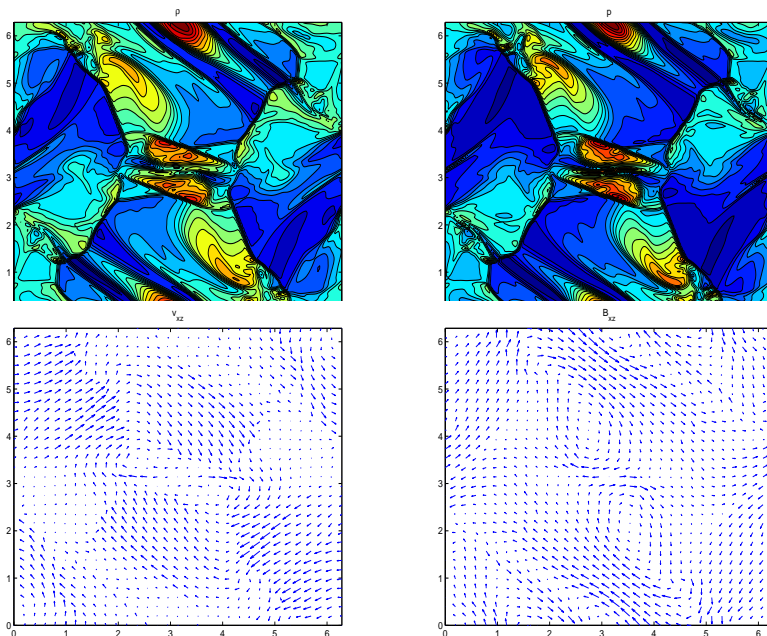

Fig. 5.8: Fourth-order solution of Orszag–Tang MHD turbulence problem with a 192×192 uniform grid at $t = 2$. There are 20 contours for density and pressure. Red –high value, blue –low value. Density range from 0.62 to 6.3, pressure range from 0.14 to 7.0. The maximum values of $|v|$ and $|B|$ are 1.6 and 2.8 respectively.
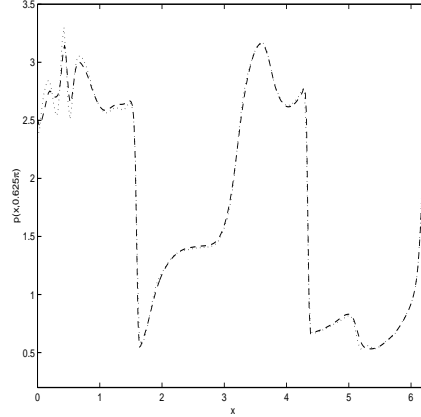
Fig. 5.9: Pressure distribution along the line $z = 0.625\pi$ at $t = 3$. Dashed line corresponds to third-order approximation with 288×288 grid points and dotted-line corresponds to fourth-order results computed with 192×192 gridpoints.

5.4. Interaction Between a Strong Shock and a High Density Cloud. This problem, introduced in [4], describes the disruption of a high density cloud by a strong shock wave. The flow is simulated over the computational domain $[0, 1] \times [0, 1]$, with 256×256 cells and open boundary conditions. The ratio of specific heats is $\gamma = 5/3$ and the initial conditions are given by the two states

$$(5.9) \quad (\rho, v_x, v_y, v_z, B_x, B_y, B_z, p)^\top = \begin{cases} (3.86859, 0, 0, 0, 0, -2.1826182, 2.1826182, 167.34)^\top & \text{for } x < 0.6 \\ (1, -11.2536, 0, 0, 0, 0.56418958, 0.56418958, 1)^\top & \text{for } x > 0.6 \end{cases},$$

separated by a discontinuity parallel to the z-axis at $x = 0.6$. To the right of the discontinuity there is a circular cloud of radius 0.15, centered at $x = 0.8$ and $z = 0.5$ with density $\rho = 10$ and $p = 1$. The solution we present at $t = 0.6$ confirms the robustness of central schemes for highly superfast flows.

As in the case of the shock tube problem, the presence of discontinuities that affect only a particular component of the system — in this case a rotational discontinuity in the y component of the magnetic field — requires the careful choice of the smoothness indicators used in the calculation of the weights of the non-oscillatory reconstruction so as to prevent oscillations. Our numerical experiments suggest the use of the average of the smoothness indicators corresponding to the y-magnetic field and the density to determine the least oscillatory stencil for the evolution of all the conserved quantities.
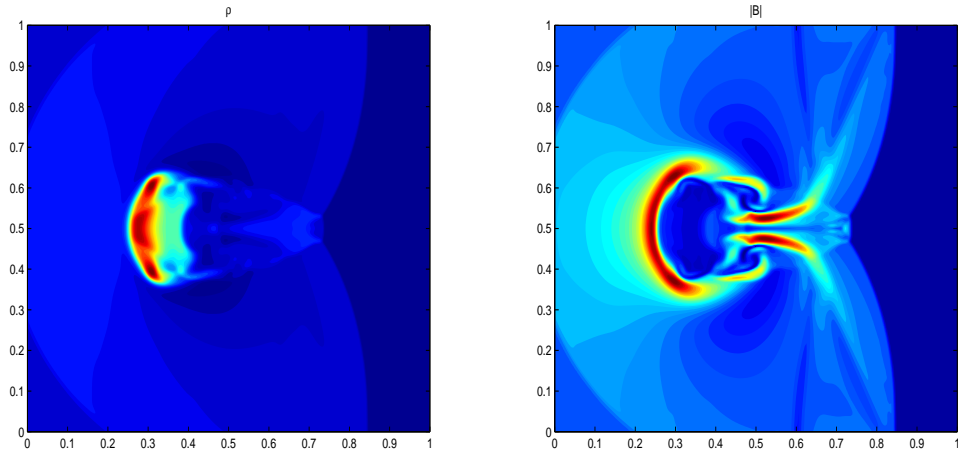
24

Fig. 5.10: Third-order solution of the interaction between a strong shock and a high density cloud obtained with a 256×256 uniform grid at $t = 0.06$, $c = 0.5$. Left: density, right: magnetic field, $|B|$.

6. Conclusions. The numerical schemes presented in this work and the results obtained with them complement those introduced in [2] and references therein, and confirm the ability of this type of black-box solvers to approximate the discontinuous solutions of ideal MHD equations accurately. The high-order semi-discrete schemes described in §2 and §3 retain the simplicity and ease of implementation of the fully-discrete *staggered* methods while adding further advantages. As the limit of the reprojection of the staggered evolution of the cell averages, the semi-discrete formulation (2.17) only requires an estimate of the maximum local speeds of propagation to evolve the solution, avoiding any detailed knowledge of the eigen structure of equations (1.1)–(1.4) and, therefore, eliminating the need for Riemann solvers. The efficiency of the semi-discrete formulation is further enhanced by the larger time step that the implementation over non-staggered grids yields and the wide range of reconstruction algorithms and ODE solvers available for its implementation. The use of these higher order routines offer advantages that extend beyond the work presented here, In particular, the ability of these schemes to compute accurate solutions over coarser grids and the possibility of applying the reconstruction algorithm dimension-by-dimension suggest these as an attractive alternative for schemes in higher space dimensions.

Our results also suggest a remarkable ability of central schemes to avoid any instability caused by the failure to satisfy the constraint $\nabla \cdot \mathbf{B} = 0$. All the results reported here have been calculated without any additional treatment for this constraint. Indeed, it can be shown that the magnetic field computed with the second-order staggered fully-discrete schemes that lead to the semi-discrete formulation presented here satisfy the condition

$$(6.1) \qquad \nabla \cdot \overline{\mathbf{B}}_{j+\frac{1}{2},k+\frac{1}{2}}^{n+1} = \nabla \cdot \overline{\mathbf{B}}_{j+\frac{1}{2},k+\frac{1}{2}}^{n},$$

where $\overline{\mathbf{B}}_{j+\frac{1}{2},k+\frac{1}{2}}^{n}$ represents the cell average of the non-oscillatory polynomial reconstruction of the cell averages $\{\overline{\mathbf{B}}_{j+p,k+q}^{n}\}_{p,q=0,1}$.

Animations of the simulations presented in §4 and §5 and sample MHD codes are available online at http://www.math.lsa.umich.edu/~jbalbas/MHD.

REFERENCES

[1] Jorge Balbás. *Non-oscillatory central schemes for the equations of ideal Magnetohydrodynamics in one- and two-space dimensions.* PhD thesis, University of California, Los Angeles., May 2004.

[2] Jorge Balbás, Eitan Tadmor, and Cheng-Chin Wu. Non-oscillatory central schemes for one- and two-dimensional MHD equations. I. *J. Comput. Phys.*, 201(1):261–285, 2004.

[3] M. Brio and C. C. Wu. An upwind differencing scheme for the equations of ideal magnetohydrodynamics. *J. Comput. Phys.*, 75(2):400–422, 1988.

[4] Wenlong Dai and Paul R. Woodward. A simple finite difference scheme for multidimensional magnetohydrodynamical equations. *J. Comput. Phys.*, 142(2):331–369, 1998.

[5] Sigal Gottlieb, Chi-Wang Shu, and Eitan Tadmor. Strong stability-preserving high-order time discretization methods. *SIAM Rev.*, 43(1):89–112 (electronic), 2001.

[6] Ami Harten, Björn Engquist, Stanley Osher, and Sukumar R. Chakravarthy. Uniformly high-order accurate essentially nonoscillatory schemes. III. *J. Comput. Phys.*, 71(2):231–303, 1987.

[7] Amiram Harten. High resolution schemes for hyperbolic conservation laws. *J. Comput. Phys.*, 49:357–393, 1983.

[8] G.-S. Jiang, D. Levy, C.-T. Lin, S. Osher, and E. Tadmor. High-resolution nonoscillatory central schemes with nonstaggered grids for hyperbolic conservation laws. *SIAM J. Numer. Anal.*, 35(6):2147–2168 (electronic), 1998.

[9] Guang-Shan Jiang and Chi-Wang Shu. Efficient implementation of weighted ENO schemes. *J. Comput. Phys.*, 126(1):202–228, 1996.

[10] Guang-Shan Jiang and Eitan Tadmor. Nonoscillatory central schemes for multidimensional hyperbolic conservation laws. *SIAM J. Sci. Comput.*, 19(6):1892–1917 (electronic), 1998.

[11] Guang-Shan Jiang and Cheng-chin Wu. A high-order WENO finite difference scheme for the equations of ideal magnetohydrodynamics. *J. Comput. Phys.*, 150(2):561–594, 1999.

[12] Alexander Kurganov and Doron Levy. A third-order semidiscrete central scheme for conservation laws and convection-diffusion equations. *SIAM J. Sci. Comput.*, 22(4):1461–1488 (electronic), 2000.

[13] Alexander Kurganov and Guergana Petrova. A third-order semi-discrete genuinely multidimensional central scheme for hyperbolic conservation laws and related problems. *Numer. Math.*, 88(4):683–729, 2001.

[14] Alexander Kurganov and Eitan Tadmor. New high-resolution central schemes for nonlinear conservation laws and convection-diffusion equations. *J. Comput. Phys.*, 160(1):241–282, 2000.

[15] Peter D. Lax. Weak solutions of nonlinear hyperbolic equations and their numerical computation. *Comm. Pure Appl. Math.*, 7:159–193, 1954.

[16] Doron Levy, Gabriella Puppo, and Giovanni Russo. Central WENO schemes for hyperbolic systems of conservation laws. *M2AN Math. Model. Numer. Anal.*, 33(3):547–571, 1999.

[17] Doron Levy, Gabriella Puppo, and Giovanni Russo. A third order central WENO scheme for 2D conservation laws. *Appl. Numer. Math.*, 33(1-4):415–421, 2000.

[18] Doron Levy, Gabriella Puppo, and Giovanni Russo. A fourth-order central WENO scheme for multidimensional hyperbolic systems of conservation laws. *SIAM J. Sci. Comput.*, 24(2):480–506 (electronic), 2002.

[19] Xu-Dong Liu and Eitan Tadmor. Third order nonoscillatory central scheme for hyperbolic conservation laws. *Numer. Math.*, 79(3):397–425, 1998.

[20] Haim Nessyahu and Eitan Tadmor. Nonoscillatory central differencing for hyperbolic conservation laws. *J. Comput. Phys.*, 87(2):408–463, 1990.

[21] S.A. Orszag and C.M Tang. Small-scale structure of two-dimensional magnetohydrodynamic turbulence. *Journal Fluid Mechanics*, 90:129–, 1979.

[22] K.G. Powell, P.L. Roe, R.S Myong, T. Gombosi, and D. de Zeeuw. An upwind scheme for magnetohydrodynamics. In *AIAA 12th Computational Fluid Dynamics Conference, San Diego, CA*, pages 661–674, June 1995.

[23] Chi-Wang Shu. Total-variation-diminishing time discretizations. *SIAM J. Sci. Statist. Comput.*, 9(6):1073–1084, 1988.

[24] Chi-Wang Shu. Essentially non-oscillatory and weighted essentially non-oscillatory schemes for hyperbolic conservation laws. In *Advanced numerical approximation of nonlinear hyperbolic equations (Cetraro, 1997)*, volume 1697 of *Lecture Notes in Math.*, pages 325–432. Springer, Berlin, 1998.

[25] Chi-Wang Shu and Stanley Osher. Efficient implementation of essentially nonoscillatory shock-capturing schemes. II. *J. Comput. Phys.*, 83(1):32–78, 1989.

[26] Hua-Zhong Tang and Kun Xu. A high-order gas-kinetic method for multidimensional ideal magnetohydrodynamics. *J. Comput. Phys.*, 165(1):69–88, 2000.

[27] Bram van Leer. Towards the ultimate conservative difference scheme. v second order sequel to godunov method. *J. Comput. Phys.*, 32:101–136, 1979.

[28] C.-C. Wu and T. Chang. Further study of the dynamics of two-dimensional MHD coherent structures–a large scale simulation. *J. of Atmospheric and Solar-Terrestrial Physics*, 95:1447–1453, 2001.